Chemical Geology 499 (2018) 84–99

Contents lists available at ScienceDirect

Chemical Geology

journal homepage: www.elsevier.com/locate/chemgeo

Platinum-group element and gold enrichment in soils monitored by chromium stable isotopes during weathering of ultramafic rocks

Javier Rivera[a,*], Martin Reich[a], Ronny Schoenberg[b], José María González-Jiménez[c], Fernando Barra[a], Thomas Aiglsperger[d], Joaquín A. Proenza[e], Sebastien Carretier[f]

[a] Department of Geology and Andean Geothermal Center of Excellence (CEGA), FCFM, Universidad de Chile, Santiago, Chile
[b] Department of Geosciences, University of Tübingen, Tübingen, Germany
[c] Departmento de Mineralogía y Petrología, Facultad de Ciencias, Universidad de Granada, Spain
[d] Luleå University of Technology Department of Civil Engineering and Natural Resources Division of Geosciences and Environmental Engineering, SE 97187 Luleå, Sweden
[e] Departament de Mineralogia, Petrologia i Geologia Aplicada, Universitat de Barcelona (UB), Martí i Franquès s/n, 08028 Barcelona, Spain
[f] GET, Université de Toulouse, CNRS, IRD, Toulouse, France

ARTICLE INFO

Editor: K. Johannesson

Keywords:
Supergene
Noble metals
Chromium isotopes
Weathering
Ultramafic rocks
Soil formation

ABSTRACT

Weathering of ultramafic rocks can lead to the formation of soil profiles with high contents of Fe, Ni, Co, platinum-group elements (PGE) and gold. Traditionally, these metal-rich soils are known as “laterites” and are formed under tropical climates and stable tectonic conditions. However, little is known about their possible development in cold/humid regions, and the factors governing PGE and gold mobility and enrichment under these weathering conditions are poorly constrained. In this study, five soil profiles developed on serpentinized, chromite-bearing ultramafic rocks at La Cabaña, located in the Coastal Range of south-central Chile (38° S) were studied by combining major and trace element geochemistry with chromium stable isotope data. The results show that the soils developed at La Cabaña have higher PGE and Au contents than the parent serpentinite rock, with ΣPGE and Au reaching up to 160 ppb and 29 ppb in a limonitic soil horizon and clay saprolite, respectively. Most soil samples have slightly negative $\delta^{53/52}Cr_{SRM979}$ values, within a range of −0.089 ± 0.012‰ to −0.320 ± 0.013‰ (average of −0.178‰), and are in agreement with previous data reported for modern soils. A noteworthy relation between $\delta^{53/52}$Cr data and PGE + Au contents is observed in the studied soil horizons, where isotopically lighter values of $\delta^{53/52}$Cr match the higher contents of PGE and gold. These results show that pedogenetic processes operating at the cold and humid La Cabaña area are capable of increasing the total PGE and Au contents of certain soil horizons. Such processes are complex and multivariate but are primarily modulated by chromite dissolution and the formation of secondary phases such as clay minerals and oxy-hydroxide phases in the soil. These findings provide evidence that important weathering and PGE + Au supergene accumulation are not only restricted to tropical latitudes, and that the chromium isotope system is a useful proxy to track surface redox process and noble metal enrichment during pedogenesis.

1. Introduction

Intense chemical weathering produces the dissolution, remobilization, and reprecipitation of elements at or near the Earth's surface, resulting in alteration and modification of primary rock materials. These processes operate together on primary minerals so as to adjust to the new environmental conditions, creating a stratified weathering profile that contains a comprehensive record of the chemical reactions involved in the soil formation (Reich and Vasconcelos, 2015). If the parent rock and its mineral constituents contains an element of economic interest (e.g., Ni, Cu, Fe, Mn, Al, and Zn), secondary in situ accumulation of metals may result in a two- to ten-fold increase in metal grades for these commodities (Reich, 2017). In particular, the pervasive weathering of ultramafic rocks can lead to weathered regoliths with one or more horizons containing exploitable reserves of Ni and Co, also known as “nickel laterites” (Freyssinet et al., 2005; Golightly, 2010; Thorne et al., 2012; Butt and Cluzel, 2013). This supergene enrichment process, also known as “lateritisation”, is responsible for residual and secondary enrichment of platinum-group elements (PGE) and gold in these deposits (Bowles, 1986; Bowles et al., 1994; Gray et al., 1996; Varajão et al., 2000; Traoré et al., 2008b; Aiglsperger et al., 2015; Aiglsperger et al., 2016; Aiglsperger et al., 2017a).

* Corresponding author.
E-mail address: jarivera@ing.uchile.cl (J. Rivera).

https://doi.org/10.1016/j.chemgeo.2018.09.008
Received 28 April 2018; Received in revised form 31 August 2018; Accepted 5 September 2018
Available online 21 September 2018
0009-2541/

Although much controversy remains, several studies have shown that PGE and Au are mobile under surficial or near-surface conditions, particularly in lateritic soils with a high presence of Fe-Mn oxy-hydroxides or clays in tropical to subtropical environments (Bowles et al., 1994; Gray et al., 1996; Sassani and Shock, 1998; van Middlesworth and Wood, 1999; Azaroual et al., 2001; Hattori and Cameron, 2004; Colombo et al., 2008; Reith et al., 2014). It is in these supergene settings where PGE mobility may even lead to the formation of secondary platinum-group minerals (PGM), as reported in laterites from Brazil, the Dominican Republic and Australia (Gray et al., 1996; Cabral et al., 2011; Aiglsperger et al., 2015; Reith et al., 2016; Aiglsperger et al., 2017a; Aiglsperger et al., 2017b). Considering that mineral assemblages in ultramafic rocks are unstable under surface conditions (Bucher et al., 2015), the weathering of ultramafic rocks and development of enriched soils on top is not only restricted to tropical climates but it may also occur in cooler climate regions (Taylor et al., 1992).

In ultramafic rocks, high PGE and Au contents are commonly linked with the abundance of accessory chromite and nickel-sulfide phases (O'Driscoll and González-Jiménez, 2016 and references therein). The noble metals are frequently found as discrete nanometer to micrometer-sized PGM or native gold inclusions within chromite whereas preferentially in solid solution in the Ni-sulfides. Thus, oxidative weathering of ultramafic rocks can result in the destruction of both chromite and Ni-sulfide host producing the liberation of PGM and metals towards the environment (Traoré et al., 2008a; Aiglsperger et al., 2015). In soils developed above mantle-derived rocks, we anticipate that the dissolution of chromite is a rate limiting step controlling the liberation of PGE and Au into soils, and overall, a first-order control on noble metal dispersion in the surface environment. In chromite, chromium is present in its trivalent oxidation state, and is released as Cr(III) aqueous species during weathering. Previous studies have shown that redox processes have a significant effect on Cr isotope fractionation. Such processes are complex and may involve several cycles of partial oxidation and partial back-reduction. On one hand, chromium isotope fractionation during oxidation from Cr(III) to Cr(VI) appears to be small, with the heavier isotope concentrating in Cr(VI) species (Zink et al., 2010). However, the reduction of Cr(VI) to Cr(III) leads to isotopic fractionation in the per mil range on the $^{53}Cr/^{52}Cr$ ratio, depending on the electron donor/acceptor involved in the reactions, preferentially partitioning the lighter Cr isotope (i.e. lower $^{53}Cr/^{52}Cr$) into Cr(III) (Ellis et al., 2002; Schoenberg et al., 2008; Zink et al., 2010; Døssing et al., 2011). Chromium released from the host rock as Cr(III) aqueous species can be then oxidized to hexavalent Cr by surface reactions with Mn oxides present in soils (Oze et al., 2007). This Cr release involves a redox cycle in which mobile species of Cr(VI) are mobilized out of the soil, while less soluble Cr(III) is preferentially retained. The overall release of Cr(VI) from the soils depends on the presence of clays or Fe-Al oxy-hydroxides, which can back-reduce Cr (VI) to Cr(III) within the soil profile if ferrous Fe, reduced S species or organic materials are present (Eary and Rai, 1987; Døssing et al., 2011). Hence, it is expected that during weathering an isotopically heavy Cr (VI) pool is released, leaving behind an isotopically light Cr(III) component in soils (Berger and Frei, 2014; Paulukat et al., 2015; D'Arcy et al., 2016; Babechuk et al., 2017; Bauer et al., 2018). This overall process is exemplified by the commonly lighter $\delta^{53/52}Cr$ signatures measured in soil horizons, and heavier $\delta^{53/52}Cr$ values reported for surface and ground waters (Frei and Polat, 2013; Berger and Frei, 2014; Frei et al., 2014; D'Arcy et al., 2016). However, slightly positive $\delta^{53/52}Cr$ values are also reported for soils, as documented by Novak et al. (2017) and Wille et al. (2018). Despite these significant advances, little is known about the geochemical factors controlling Cr isotope fractionation during weathering of chromite, and the potential use of $\delta^{53/52}Cr$ signatures to track noble metal enrichment in soils.

In this paper, we aim to evaluate the geochemical controls on PGE and Au enrichment during oxidative weathering of chromite-bearing ultramafic rocks. Also, we test if noble metal enrichment in soils developed on these types of rocks can be monitored using the chromium stable isotope system. To achieve this goal we studied five soil profiles developed above chromite-bearing serpentinized ultramafic rocks at La Cabaña in South-Central Chile. Our approach combined major and trace element geochemistry with Cr stable isotope data along soil profiles of variable thickness and degrees of weathering. Chromium isotopes were used here as a soil redox proxy due to the well-documented fractionation of Cr isotopes during oxidation-reduction processes (Ellis et al., 2002; Schoenberg et al., 2008; Frei et al., 2009; Zink et al., 2010). Our results show an important correspondence between the measured $\delta^{53/52}Cr$ and PGE and Au contents in soil, suggesting that noble metal enrichment in lateritic soils may be influenced by similar processes affecting the Cr redox cycle during pedogenesis.

2. Geological and climatic setting

The La Cabaña area is located 60 km north-west of the city of Temuco (Fig. 1a) and is one of the largest known occurrences of ultramafic rocks preserved in the Late Paleozoic Accretionary Complex of the Coastal Range of south-central Chile (locally named Nahuelbuta Mountains). This fossil accretionary complex comprises different metamorphic rock units separated in two metamorphic belts called the Western Series and Eastern Series. The Western Series is mainly composed of deformed metagraywackes, metapelites, metabasites and several small serpentinite bodies (Hervé, 1988; Hervé et al., 2013; González-Jiménez et al., 2014a; González-Jiménez et al., 2016; González-Jiménez et al., 2017). The climate of the Coastal Range at 38° S is characterized by a mean annual temperature around 13 °C and a mean annual precipitation (MAP) above 1000 mm per year in coastal areas and lowlands (Fig. 1b). Precipitation increases with altitude in the Nahuelbuta Range (Garreaud et al., 2016), and is most intense during the fall and winter seasons (March–August). This cool and humid climate favors the growth of abundant vegetation represented by native forests and patches of exotic plantations including *Pinus radiata* and *Eucalyptus*.

At La Cabaña, metamorphosed ultramafic rocks crop out in six main bodies, known as Centinela Bajo Norte, Centinela Bajo Sur, Encanto River, Loma Gúzman, Lavanderos and Mina de Talco (Fig. 2; González-Jiménez et al., 2016). Centinela Bajo Norte and Sur are the largest bodies in this area and are hosted in micaceous schists also bearing metavolcanic rocks (Romero et al., 2017). These two bodies consist of isolated blocks of massive chromite-bearing and clinopyroxene-poor meta-dunite (< 60% of olivine replaced by lizardite) embedded in a matrix of schistose, locally mylonitic, antigorite (Atg) serpentinite (González-Jiménez et al., 2017). In these rocks chromite is frequently found as an accessory mineral that locally may be concentrated as schlieren, veins or chromitite pods (> 50 cm) with > 90% of modal chromite (Barra et al., 1998; Höfer et al., 2001; Barra et al., 2014; González-Jiménez et al., 2014a). The regional retrograde metamorphism has affected the chromite grains, giving rise to zoning characterized by relic cores preserving the magmatic signature with an internal rim of Fe^{+2}-rich porous chromite surrounded by external rim of Fe^{+3}-rich homogenous chromite (i.e., ferrian chromite) and/or Cr-magnetite (Barra et al., 2014; González-Jiménez et al., 2016). The chromitite pods contain ~250 ppb average PGE + Au, whereas serpentinites contain from 10 to 30 ppb of PGE + Au (González-Jiménez et al., 2014a; González-Jiménez et al., 2016). This mineralization is associated with micrometer-sized inclusions (< 25 μm) of PGMs [mainly laurite (RuS_2), erlichmanite (OsS_2) and irarsite (IrAsS)], native gold (Au^0), PGE-bearing sulfides [millerite (NiS), violarite ($FeNiS_4$)] and arsenides [maucherite ($Ni_{11}As_8$) and gersdorffite (NiFeAs)], which are found in unaltered cores and alteration rims of chromite (González-Jiménez et al., 2014a; González-Jiménez et al., 2016).

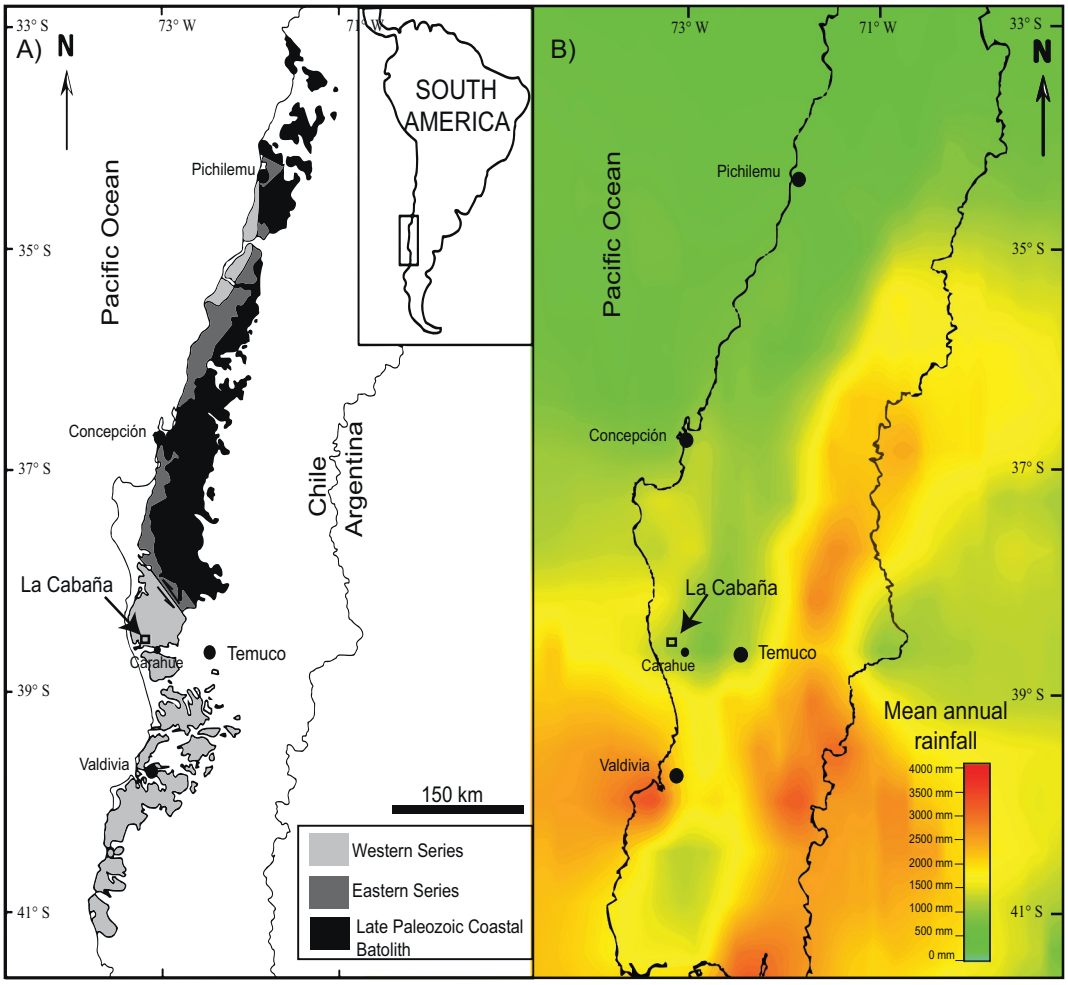

Fig. 1. a) Simplified geological map of south-central Chile showing the location of the study area. Modified from Barra et al. (2014) and González-Jiménez et al. (2016). b) Precipitation map of south-central Chile, constructed from interpolated data collected from the CR2 database (http://explorador.cr2.cl).

3. Samples and methods

3.1. Soil profile samples

Thirty samples were collected from five soil profiles developed above the ultramafic body of Centinela Bajo (Fig. 2). Samples were taken using a plastic soil probe (hand tube) and a plastic shovel to avoid metal contamination. Each sample (1.5–3 kg each) was collected from representative soil horizons and included, from bottom to top, bedrock (serpentinites), green coarse saprolite, gray or pale clay saprolite, yellow to brownish, sometimes reddish limonitic soil horizons (B horizons), and brownish to dark brownish uppermost horizons (A horizons). The sampled soil profiles have variable thickness, from 1.2 m (LC 1) up to 12 m (P.FOR), and are mainly developed above schistose serpentinite with antigorite ± talc, accessory chromite and Cr-magnetite grains, and antigorite ± tremolite, talc and Cr-magnetite bearing serpentinite.

3.2. Mineral separation and bulk geochemistry

Mineral characterization of the samples was undertaken using a combination of X-ray diffraction (XRD), hydroseparation (HS) and scanning electron microscopy (SEM) techniques. XRD analyses were carried out using a Bruker D8 Advance Bragg-Brentano instrument in the Department of Physics, University of Chile, using CuKα1 radiation. The powdered samples (< 200 μm) were scanned from 4° to 80° 2θ with a step size of 0.02° and measuring time of 0.1 s per step, and operating conditions of 40 kV and 30 mA. Additionally, heavy mineral concentrates were obtained for two samples from profile LC 4 at the Hydroseparation Laboratory at the University of Barcelona, using a computer-controlled HS device CNT HS11, following the methodology by Aiglsperger et al. (2015). Prior the separation, the samples were carefully crushed with an agate mortar, homogenized, and then wet-sieved into different size fractions using plastic screens. Mineral separates of size fractions < 30 μm and 30–50 μm were obtained, using between 300 and 500 g per fraction. The final heavy mineral concentrates were mounted as polished monolayer resin blocks. Also, mineral concentrates of selected samples were obtained for SEM observation. The samples were wet-sieved using plastic screens, panned, selected for concentrates, mounted with epoxy in cylindrical resin blocks and polished. Subsequently, concentrates were studied with a FEI Quanta 250 SEM at the Andean Geothermal Center of Excellence (CEGA), University of Chile, equipped with energy dispersive spectrometer (EDS) and a back-scattered electron (BSE) detector. Also, two polished monolayers were inspected using a JEOL JSM-7100 field emission (FE) SEM at the Serveis Científics i Tecnòlogics, University of Barcelona, Spain.

Soil samples were analyzed for major and trace elements in the Australian Laboratory Services (ALS, Geochemistry) using a combination of inductively coupled plasma atomic emission spectrometry (ICP-AES), X-ray fluorescence (XRF) and inductively coupled plasma mass spectrometry (ICP-MS) techniques. PGE and Au contents were determined at Genalysis Ltd. (Maddington, Western Australia) by fire assay with nickel sulfide collection and measured by ICP-MS (detection

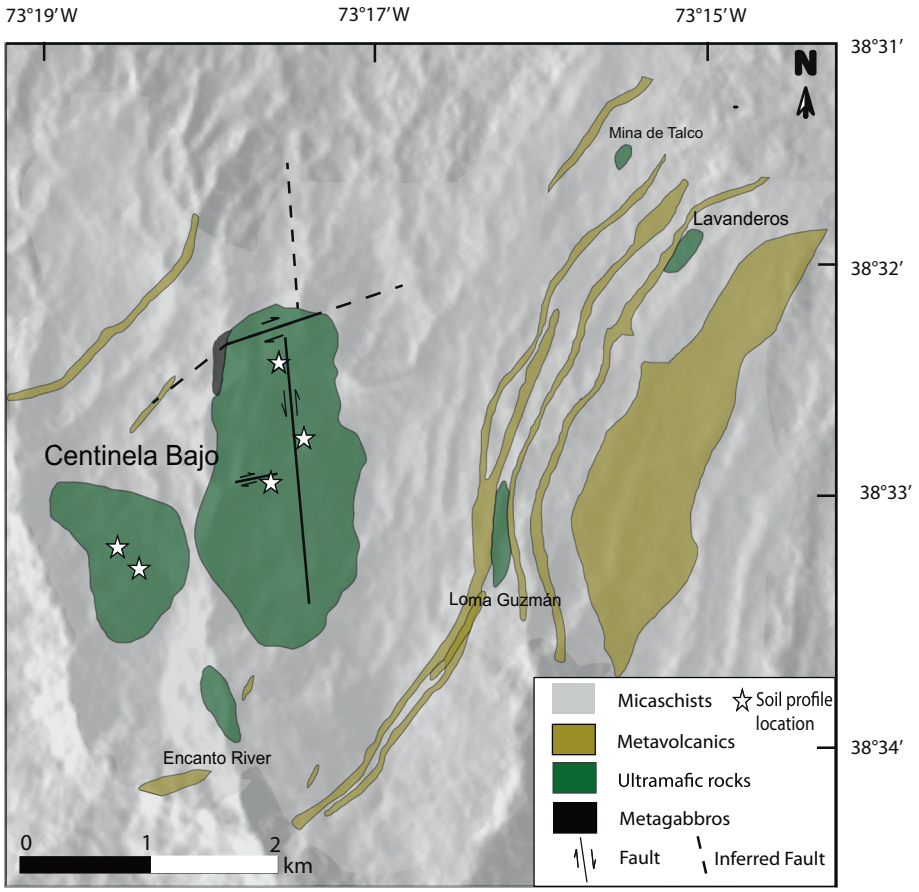

Fig. 2. Geological map of the La Cabaña area in southern Chile, modified from González-Jiménez et al. (2016). The soil profile locations are showed as stars, from north to south, profiles LC 2, LC 1, LC 4, P.CBS and P.FOR, respectively.

limits between 1 and 5 ppb).

3.3. Chromium stable isotopes

Twenty-two samples from five soil profiles were crushed using an agate mortar, and 20 mg aliquots were taken for digestion. Samples were digested in pressurized bombs in an oven at a temperature of 220 °C for 4 days using a mixture of HF + HNO_3 to ensure dissolution of resistant phases such as chromite. After opening the bombs and drying down the samples, the residue was refluxed in 6 M HCl and the bombs placed back into the oven at 220 °C for 24 h to dissolve fluorides that formed during the digestion. After cooling, the samples were transferred to 15 mL Savillex Beakers®, dried down on a hot plate, and then dissolved and stored in 10 mL of 6 M HCl. Prior to chemical separation, volumetrically-calibrated aliquots of each sample were taken at a Cr concentration of 1.5 μg, followed by the addition of 68.2 μL of ^{54}Cr-^{50}Cr double spike solution and overnight homogenization on a hot plate at 85 °C. The addition of a double spike with a known sample-spike ratio allows to correct for any chemical fractionation that may occur during chemical purification of Cr from the matrix (Schoenberg et al., 2008).

The purification of Cr from the matrix elements was achieved using the protocol described by Schoenberg et al. (2016), and involves chemical separation by three different ion exchange chromatographic columns. The first column is prepared with Biorad Dowex® AG1-×8 anionic porous resin and allows to remove Fe from the samples. After that, two steps of chemical purification with BioRad Dowex® AG50W-×8 cation resin were performed to purify Cr from the residual matrix elements. Samples processed using this chemical procedure has been shown to produce matching Cr isotope ratios (Schoenberg et al., 2016; Babechuk et al., 2017; Wille et al., 2018).

All Cr isotope ratio measurements were performed using a ThermoFisher Scientific NeptunePlus multiple-collector inductively coupled plasma mass spectrometer (MC-ICP-MS) at the Isotope Geochemistry Laboratory of the Department of Geosciences, University of Tübingen. The instrument was run in medium resolution mode to avoid polyatomic interferences from mainly $^{40}Ar^{12}C^+$ on $^{52}Cr^+$, $^{40}Ar^{14}N^+$ on $^{54}Cr^+$ and $^{40}Ar^{16}O^+$ on the interference monitor $^{56}Fe^+$, respectively (Schoenberg et al., 2008; Schoenberg et al., 2016). Data are reported in the δ notation in per mil (‰) relative to the isotopically certified international reference material NIST SRM979:

$$\delta^{53/52}Cr = [(^{53}Cr/\ ^{52}Cr_{sample})/(^{53}Cr/\ ^{52}Cr_{SRM979}) - 1] \times 1000$$

4. Results

4.1. Mineral characterization of soil profiles

XRD analyses of soil samples show the presence of chlorite (clinochlore and chamosite), kaolinite, smectite group minerals (nontronite), magnetite, goethite and Fe-Al-Mn oxyhydroxide phases. SEM observations of heavy mineral concentrates show the presence of chromite ($FeCr_2O_4$), ilmenite ($FeTiO_3$), zircon ($ZrSiO_4$), monazite ((La, Ce, Nd, Th)PO_4), rutile (TiO_2) and sulfides, including acanthite (Ag_2S), chalcopyrite ($CuFeS_2$), covellite (CuS) and pyrrhotite ($Fe_{1-x}S$). Two PGM grains were identified in the hydro-separated concentrate of sample LC4-4, one sperrylite ($PtAs_2$) grain of 25 μm and a 15 μm Ru-Ir-Os-Pt-Fe-Ni grain (Fig. 3). Also, micrometer-sized platinum-bearing particles (Pt^0 or Pt-Fe) were observed in the rim of porous chromite grains. Gold grains were found in the 30–50 μm fraction and one grain was found in the < 30 μm fraction, showing an average content of 80 wt% Au and

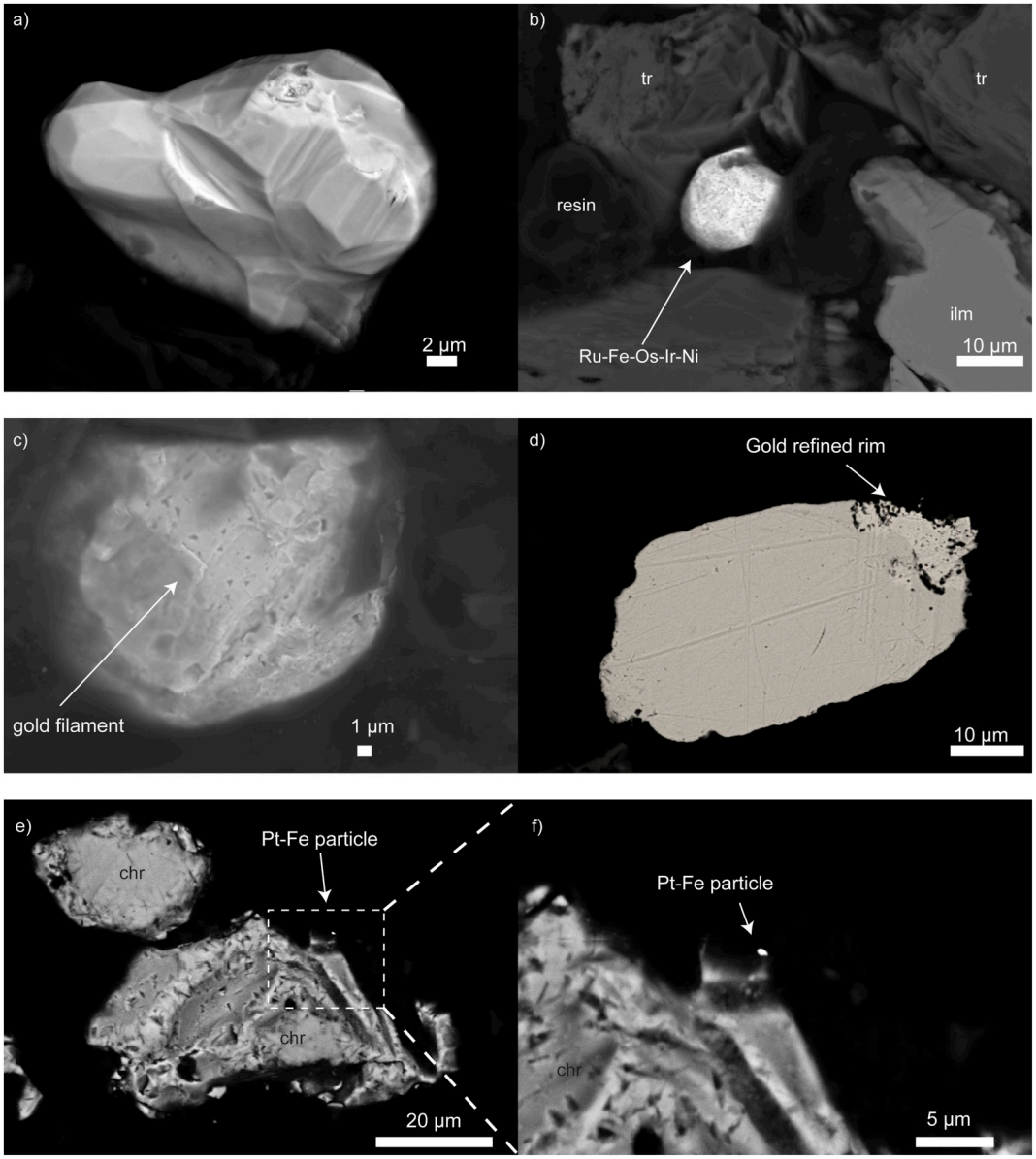

Fig. 3. FESEM and SEM images of PGM and Au grains found in polished monolayers of a hydro-separated concentrate from sample LC4–4. a) sperrylite ($PtAs_2$); b) Ru-Fe-Os-Ir-Ni grain surrounded by tremolite (tr) and ilmenite (ilm) grains; c) native gold grain with obscure triangle patch zones and small gold filament; d) native gold grain with a gold-refined rim in which triangle shaped patch zones are noted (80 wt% Au and 20 wt% Ag measured at the grain center using EDS). e) Porous chromite grain with a Pt-Fe nanoparticle in the rim; f) Zoom of the chromite grain and the Pt-Fe nanoparticle in e). (For interpretation of the references to colour in this figure legend, the reader is referred to the web version of this article.)

20 wt% Ag (measured by SEM-EDS). In some cases, a few wt% Cu and Pd were found in the Au grains. The rims of Au grains show Ag depletion and Au refining, characterized by patchy textures and small filaments (Fig. 3). Additionally, micrometer-sized native Au particles were observed encapsulated within tremolite grains.

4.2. Bulk soil geochemistry

The major and trace element chemical analyses of soil and saprolite samples from selected soil profiles are shown in Table 1. Figs. 4 and 5 display the chemical variations of selected major ($Fe_2O_{3(t)}$, MgO, Al_2O_3, SiO_2), minor (Cr_2O_3, TiO_2, MnO) and PGE (Pt, Pd and Ru) + Au as a function of depth for two representative soil profiles, P.FOR and LC-4. In general, upward enrichment (retention trend) is noted for Fe and Al, and a progressive loss of Mg and Si is observed in the upper horizons, contrasting chemically the saprolite with the upper soil horizons. In profile P.FOR (Fig. 4), these differences are well stablished, where the serpentinite and saprolite have > 20 wt% MgO, while the limonitic and organic matter rich upper soil horizons show < 5 wt% MgO. This geochemical shift is coupled with the increase of Fe_2O_3 content up to 35.4 wt% and SiO_2 depletion to 20.7 wt% (Fig. 4). These variations correspond with an increase of immobile elements such as Nb, Sc, Ti and Zr in upper soil horizons (see Table 1). Soil profile LC4 shows similar major element trends with depth, although variations are subtler than profile P.FOR (Figs. 4 and 5). Profiles LC1 and LC2, have a similar trend with depth, but with subtler variations than profile P.FOR. Soil profile P.CBS has much less prominent chemical differences of major elements within soil horizons, suggesting a lesser degree of weathering (Table 1).

Chromium (Cr_2O_3) contents in soil profile P.FOR (Fig. 4) vary from 0.14–0.28 wt% in bedrock and coarse saprolite, increasing to 2.77 wt% in a mottled limonitic horizon (sample P.FOR-2, Table 1). This Cr-rich horizon also contains higher contents of metals such as Co, Cu, Mn, PGE,

Table 1
Major, minor and trace element content of soil samples from profiles LC1, LC2, LC4, P.FOR and P.CBS. Included ultramafic index of alteration (UMIA, in %) and index of laterisation (IOL, in %). Major elements are reported in weight percent (wt%), trace elements in parts per million (ppm) and PGE + Au in parts per billion (ppb).

	LC1-1	LC1-2	LC1-3	LC1-4	LC2-1	LC2-2	LC2-4	LC2-5	LC4-1	LC4-2	LC4-3	LC4-4
Sample type	Soil	Soil	Soil	Coarse saprolite	Soil	Soil	Clay saprolite	Clay saprolite	Soil	Soil	Soil	Clay saprolite
wt%												
SiO_2	44.40	33.70	33.60	39.60	26.70	28.30	27.20	35.10	34.10	37.00	40.90	45.70
Al_2O_3	14.10	19.00	2.84	0.44	19.30	19.10	15.60	19.15	15.25	18.30	18.40	8.89
Fe_2O_3	8.91	16.45	18.75	9.81	15.45	17.00	20.30	8.49	12.55	12.45	9.79	13.95
CaO	0.71	0.36	0.03	0.03	1.26	1.83	1.55	19.95	3.94	3.92	4.50	7.95
MgO	7.37	6.65	28.60	34.30	7.40	10.60	14.25	10.60	9.96	11.85	12.35	13.95
Na_2O	0.86	0.49	< 0.01	< 0.01	0.32	0.37	0.27	0.02	0.38	0.25	0.16	0.02
K_2O	0.66	0.53	0.04	0.03	0.21	0.18	0.13	0.03	0.12	0.11	0.05	0.02
Cr_2O_3	0.87	0.62	0.62	0.54	0.42	0.67	1.19	0.23	0.50	0.48	0.46	0.52
TiO_2	1.33	1.28	0.09	< 0.01	1.06	0.92	0.66	0.14	0.59	0.50	0.27	0.08
MnO	0.07	0.05	0.13	0.16	0.15	0.17	0.19	0.25	0.10	0.09	0.08	0.08
P_2O_5	0.08	0.08	0.02	< 0.01	0.06	0.05	0.05	< 0.01	0.06	0.02	0.01	< 0.01
SrO	0.01	0.01	< 0.01	< 0.01	< 0.01	0.01	< 0.01	< 0.01	< 0.01	< 0.01	< 0.01	< 0.01
BaO	0.02	0.02	< 0.01	< 0.01	0.01	0.01	< 0.01	< 0.01	< 0.01	< 0.01	< 0.01	< 0.01
LOI	21.40	22.70	14.65	13.50	26.20	21.50	18.55	5.58	21.90	15.75	13.10	8.89
Total	100.79	101.94	99.37	98.41	98.54	100.71	99.94	99.54	99.45	100.72	100.07	100.05
UMIA	17.39	28.50	10.27	4.17	31.29	28.58	25.79	22.15	21.88	22.06	19.67	13.62
IOL	34.13	51.27	39.12	20.56	56.55	56.06	56.89	44.05	44.91	45.39	40.80	33.32
ppm												
Ba	203.0	142.5	8.3	6.5	58.5	58.3	40.2	5.5	40.1	38.1	31.4	6.8
Ce	19.3	32.9	13.8	1.5	29.1	42.7	40.6	2.6	8.1	5.3	3.6	5.6
Cr	5050	3520	3500	3730	2930	4200	7310	1640	3350	2960	3190	3480
Cs	4.36	2.88	0.09	0.01	1.32	1.36	0.92	0.07	0.67	0.60	0.42	0.16
Dy	1.74	2.66	1.95	1.33	1.87	2.26	1.67	1.67	0.95	0.74	0.70	0.55
Er	1.21	1.81	1.23	0.70	1.06	1.43	0.98	0.98	0.66	0.53	0.34	0.33
Eu	0.39	0.67	0.56	0.22	0.59	0.68	0.55	0.48	0.20	0.23	0.22	0.07
Ga	22.6	25.5	3.0	0.4	21.7	19.5	13.7	12.1	14.2	15.7	11.5	5.9
Gd	1.79	2.54	1.98	1.21	1.84	2.09	1.56	1.27	0.86	0.72	0.66	0.38
Hf	5.9	5.3	0.4	< 0.2	3.9	3.9	6.4	0.2	1.6	1.6	0.8	0.2
Ho	0.34	0.51	0.41	0.31	0.42	0.45	0.35	0.36	0.21	0.17	0.13	0.12
La	9.50	7.70	3.70	3.90	5.60	5.30	3.70	4.30	3.70	2.70	3.30	0.80
Lu	0.21	0.33	0.17	0.08	0.17	0.22	0.15	0.18	0.09	0.07	0.06	0.05
Nb	9.4	7.6	0.6	< 0.2	5.5	4.6	3.8	0.2	2.8	2.3	1.2	0.3
Nd	8.40	9.80	7.20	4.80	7.50	8.80	6.90	4.10	3.60	3.40	3.10	1.10
Pr	2.21	2.17	1.57	1.30	1.71	1.85	1.40	0.99	0.89	0.72	0.69	0.21
Rb	30.6	22.8	0.7	0.4	7.4	6.6	4.7	0.3	4.0	3.4	1.9	0.5
Sm	2.10	2.96	2.08	0.86	2.16	2.54	1.96	0.97	0.88	0.72	0.80	0.38
Sn	3.0	2.0	1.0	1.0	2.0	2.0	2.0	1.0	1.0	1.0	1.0	1.0
Sr	73.8	42.5	1.8	1.6	43.1	53.2	34.0	5.8	25.0	18.0	11.2	1.9
Ta	0.6	0.5	0.1	< 0.1	0.3	0.3	0.5	0.1	0.2	0.2	0.1	< 0.1
Tb	0.29	0.47	0.37	0.23	0.30	0.42	0.28	0.23	0.15	0.13	0.12	0.07
Th	4.90	6.97	0.50	< 0.05	4.35	4.14	3.32	0.14	1.16	1.78	0.88	0.13
Tm	0.18	0.29	0.18	0.09	0.16	0.20	0.16	0.18	0.10	0.09	0.05	0.03
U	1.66	1.72	0.17	< 0.05	1.21	1.21	0.90	< 0.05	0.50	0.51	0.32	0.11
V	< 5	44	< 5	< 5	188	< 5	< 5	143	86	104	62	30
W	2.0	4.0	1.0	1.0	2.0	2.0	1.0	4.0	2.0	2.0	1.0	2.0
Y	9.90	11.50	8.80	9.20	8.40	8.60	6.50	9.80	5.60	4.00	3.30	2.60
Yb	1.39	2.18	1.44	0.53	1.14	1.45	1.18	1.16	0.63	0.57	0.38	0.36
Zr	229.0	199.0	13.0	2.0	147.0	139.0	100.0	5.0	58.0	61.0	32.0	8.0

(*continued on next page*)

Table 1 (*continued*)

	LC1-1	LC1-2	LC1-3	LC1-4	LC2-1	LC2-2	LC2-4	LC2-5	LC4-1	LC4-2	LC4-3	LC4-4
Sample type	Soil	Soil	Soil	Coarse saprolite	Soil	Soil	Clay saprolite	Clay saprolite	Soil	Soil	Soil	Clay saprolite
Ag	< 0.5	< 0.5	< 0.5	< 0.5	< 0.5	< 0.5	< 0.5	< 0.5	< 0.5	< 0.5	< 0.5	< 0.5
As	9.0	26.0	25.0	26.0	17.0	23.0	28.0	< 5	5.0	6.0	< 5	5.0
Cd	< 0.5	< 0.5	< 0.5	< 0.5	< 0.5	< 0.5	< 0.5	< 0.5	< 0.5	< 0.5	< 0.5	< 0.5
Co	50.0	68.0	157.0	152.0	62.0	105.0	202.0	58.0	56.0	56.0	62.0	44.0
Cu	27.0	45.0	12.0	1.0	49.0	55.0	54.0	5.0	29.0	31.0	44.0	121.0
Li	30.0	20.0	0.0	0.0	40.0	30.0	20.0	20.0	10.0	20.0	20.0	0.0
Mo	< 1	< 1	< 1	< 1	< 1	< 1	< 1	< 1	< 1	< 1	< 1	< 1
Ni	678	940	1880	3590	541	839	1080	428	501	604	660	536
Pb	12.0	12.0	5.0	< 2	9.0	10.0	6.0	< 2	5.0	3.0	< 2	3.0
Sc	14.0	26.0	19.0	8.0	20.0	29.0	29.0	31.0	27.0	28.0	32.0	34.0
Tl	< 10	< 10	10.00	< 10	< 10	< 10	< 10	10.00	< 10	< 10	< 10	10.00
Zn	160.0	120.0	66.0	65.0	88.0	115.0	144.0	57.0	94.0	68.0	53.0	37.0
ppb												
Os	< 5	< 5	5	5	< 5	< 5	< 5	< 5	< 5	< 5	< 5	< 5
Ir	4	4	7	5	< 2	3	3	3	< 2	2	< 2	< 2
Ru	5	6	17	9	3	6	8	8	< 2	4	5	4
Rh	< 2	1	4	2	1	1	2	2	< 2	2	2	3
Pt	4	7	18	12	10	15	22	23	12	17	20	38
Pd	4	5	8	2	11	23	23	87	28	44	63	72
Au	8	9	9	4	9	8	8	6	8	11	17	29
ΣPGE + AU	25	32	68	39	34	56	66	129	48	80	107	146
ΣREE (ppm)	49.05	66.99	36.64	17.06	53.62	70.39	61.44	19.47	21.02	16.09	14.15	10.05
τCr vs Sc	0.37	−0.48	−0.28	0.48	0.60	0.76	2.12	−0.44	−0.59	−0.62	−0.68	−0.66
τCr vs Ti	−0.95	−0.96	−0.44	0.32	−0.94	−0.88	−0.71	−0.73	−0.86	−0.84	−0.72	0.06

	LC4-PR	LC4-5	P.FOR-1	P.FOR-2	P.FOR-3	P.FOR-4	P.CBS-1	P.CBS-2	P.CBS-3	P.CBS-4	P.CBS-5	P.CBS-6
Sample type	Bedrock	Fe-mn concretion	Soil	Soil	Soil	Coarse saprolite	Coarse saprolite	Saprolite	Saprolite	Soil	Soil	Soil
wt%												
SiO_2		9.85	22.50	20.70	35.00	40.60	39.61	30.91	43.21	45.24	43.92	43.03
Al_2O_3		8.39	23.40	18.25	6.41	2.30	6.21	18.60	15.14	15.01	11.29	14.48
Fe_2O_3		56.66	25.70	35.40	11.10	10.05	13.33	12.40	8.05	7.27	7.67	7.69
CaO		0.07	0.50	0.04	0.03	0.07	0.88	0.20	9.37	10.85	7.17	7.08
MgO		0.76	3.66	4.48	29.50	33.70	25.23	23.29	16.78	14.41	21.41	17.13
Na_2O		0.07	0.05	< 0.01	< 0.01	< 0.01	0.07	0.01	0.52	0.55	0.44	0.57
K_2O		0.11	0.07	0.02	0.03	0.03	0.02	0.02	0.08	0.09	0.05	0.07
Cr_2O_3		0.42	1.17	2.77	0.58	0.85	0.64	0.49	0.32	0.22	0.41	0.28
TiO_2		0.55	0.79	0.30	0.05	0.06	0.03	0.15	0.15	0.21	0.06	0.12
MnO		2.88	0.18	0.50	0.40	0.17	0.22	0.31	0.35	0.15	0.12	0.12
P_2O_5		0.03	0.06	0.04	0.01	< 0.01	0.02	0.02	0.02	0.02	0.02	0.02
SrO		< 0.01	< 0.01	< 0.01	< 0.01	< 0.01	< 0.01	< 0.01	0.02	0.02	< 0.01	0.01
BaO		0.01	0.01	< 0.01	< 0.01	< 0.01	< 0.01	< 0.01	0.01	0.01	< 0.01	0.01
LOI		21.00	22.60	15.95	13.40	11.50	14.45	14.20	6.78	6.55	7.94	10.00
Total		100.80	100.69	98.45	96.51	99.33	100.70	100.60	100.80	100.60	100.50	100.60
UMIA		70.51	45.63	46.79	9.15	5.35	10.10	19.23	14.91	14.79	11.17	14.28
IOL		86.85	68.58	72.16	33.35	23.32	33.03	50.07	34.92	33.00	30.15	34.00
ppm												
Ba			73.4	31.0	19.3	2.8						
Ce			54.0	46.0	2.7	< 0.5						

(*continued on next page*)

Table 1 (*continued*)

	LC4-PR	LC4-5	P.FOR-1	P.FOR-2	P.FOR-3	P.FOR-4	P.CBS-1	P.CBS-2	P.CBS-3	P.CBS-4	P.CBS-5	P.CBS-6
Sample type	Bedrock	Fe-mn concretion	Soil	Soil	Soil	Coarse saprolite	Coarse saprolite	Saprolite	Saprolite	Soil	Soil	Soil
Cr			7040	> 10,000	3880	5230						
Cs			0.79	0.30	0.03	< 0.01						
Dy			3.51	2.52	1.61	0.65						
Er			1.83	1.75	1.02	0.40						
Eu			0.97	0.85	0.34	0.09						
Ga			24.1	16.5	6.8	2.6						
Gd			3.22	3.19	1.29	0.37						
Hf			3.9	1.2	< 0.2	< 0.2						
Ho			0.70	0.59	0.40	0.13						
La			6.90	14.80	4.60	1.00						
Lu			0.28	0.34	0.15	0.07						
Nb			4.1	1.3	0.7	< 0.2						
Nd			12.90	18.20	4.60	1.00						
Pr			2.70	4.03	1.17	0.24						
Rb			2.8	1.1	0.4	0.2						
Sm			3.38	3.35	1.18	0.34						
Sn			2.0	1.0	1.0	1.0						
Sr			9.1	1.4	0.6	0.3						
Ta			0.3	0.1	< 0.1	< 0.1						
Tb			0.55	0.43	0.25	0.08						
Th			4.32	1.17	< 0.05	< 0.05						
Tm			0.30	0.29	0.15	0.06						
U			1.35	0.48	0.05	< 0.05						
V			< 5	< 5	< 5	< 5						
W			3.0	1.0	7.0	1.0						
Y			13.10	17.10	9.30	3.30						
Yb			1.98	1.88	1.05	0.43						
Zr			140.0	45.0	6.0	2.0						
Ag			< 0.5	< 0.5	< 0.5	< 0.5						
As			18.0	33.0	18.0	< 5						
Cd			< 0.5	< 0.5	< 0.5	< 0.5						
Co			128.0	396.0	480.0	112.0						
Cu			62.0	60.0	26.0	9.0						
Li			10.0	10.0	0.0	0.0						
Mo			< 1	< 1	< 1	< 1						
Ni			727	1235	2370	1690						
Pb			10.0	3.0	< 2	< 2						
Sc			47.0	69.0	35.0	9.0						
Tl			< 10	< 10	< 10	< 10						
Zn			94.0	141.0	21.0	77.0						
ppb												
Os	< 5	< 5	< 5	< 5	< 5	< 5	< 5	< 5	< 5	< 5	< 5	< 5
Ir	4	1	4	3	5	< 2	5	< 5	< 5	< 5	< 5	< 5
Ru	5	< 2	15	39	30	8	< 2	< 2	< 2	< 2	< 2	< 2
Rh	1	< 2	5	10	5	1	< 2	< 2	< 2	< 2	< 2	< 2
Pt	5	< 1	20	53	27	6	< 1	< 1	< 1	20	< 1	< 1
Pd	2	1	16	55	21	10	22	18	10	8	7	8
Au	5	2	15	18	9	6	2	< 2	2	< 2	< 2	< 2
ΣPGE + AU	22	4	75	178	97	31	29	18	12	28	7	8
ΣREE (ppm)			93.22	98.22	20.51	4.86						
τCr vs Sc			−0.52	−0.23	−0.68	0.82						
τCr vs Ti		−0.94	−0.88	−0.25	−0.05	0.15	0.74	−0.73	−0.83	−0.91	−0.44	−0.81

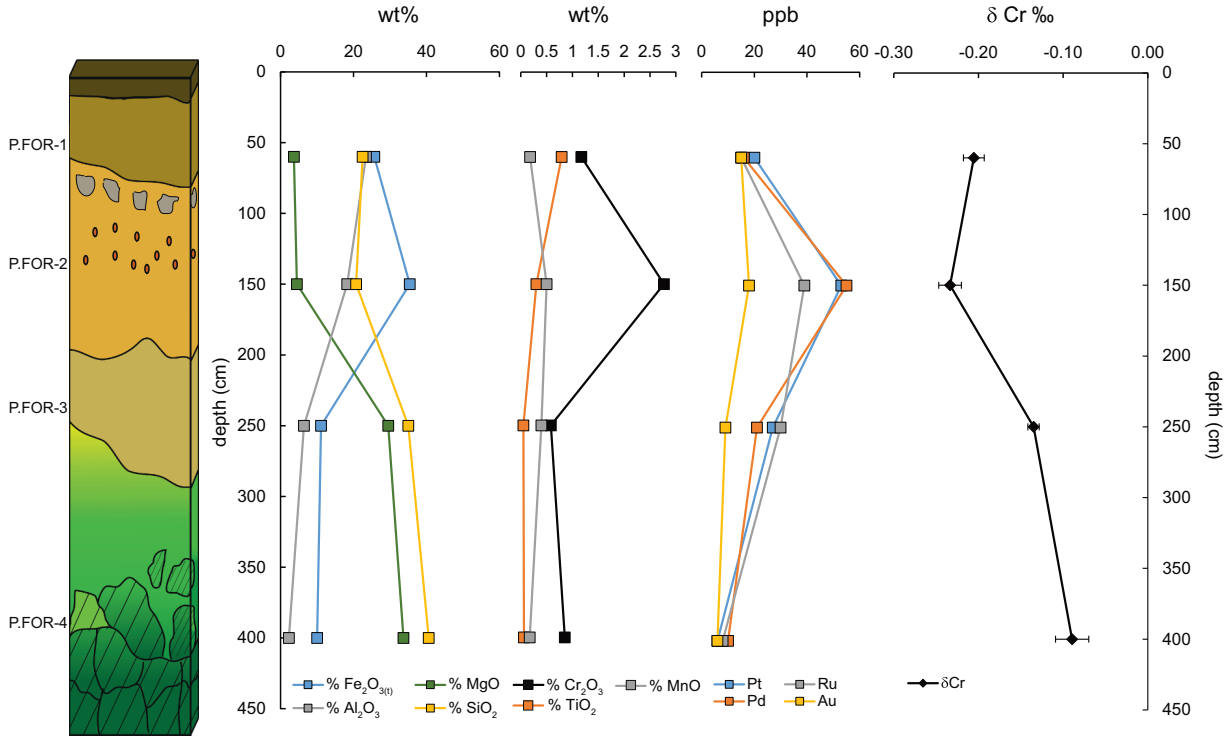

Fig. 4. Bulk major ($Fe_2O_{3\ TOTAL}$, MgO, Al_2O_3 and SiO_2), minor (Cr_2O_3 TiO_2 and MnO) and trace element (Ru + Pt + Pd + Au) contents for the P.FOR soil profile, located in the south part of Centinela Bajo. Additionally, the $\delta^{53/52}$Cr values are shown on the right.

REE and Sc (Fig. 4 and Table 1). Titanium (TiO_2), on the other hand, shows an upward increase in soil profiles, with a few hundred ppm in the bedrock and reaching up to 1.3 wt% in the upper horizons (Fig. 4). Phosphorus (P_2O_5) and Zr contents follow the same trend reported for Ti (Table 1). In contrast, Mn contents do not follow a clear pattern with depth, although this element is enriched in limonitic horizons in profiles LC-1 and P.FOR (Fig. 4 and Table 1). In profile LC4 Mn content does not vary with depth, although a Fe-Mn concretion with 2.88 Mn wt% is present between the saprolite and the upper horizons (Table 1). Nickel contents decrease towards the surface, showing a clear loss of this metal

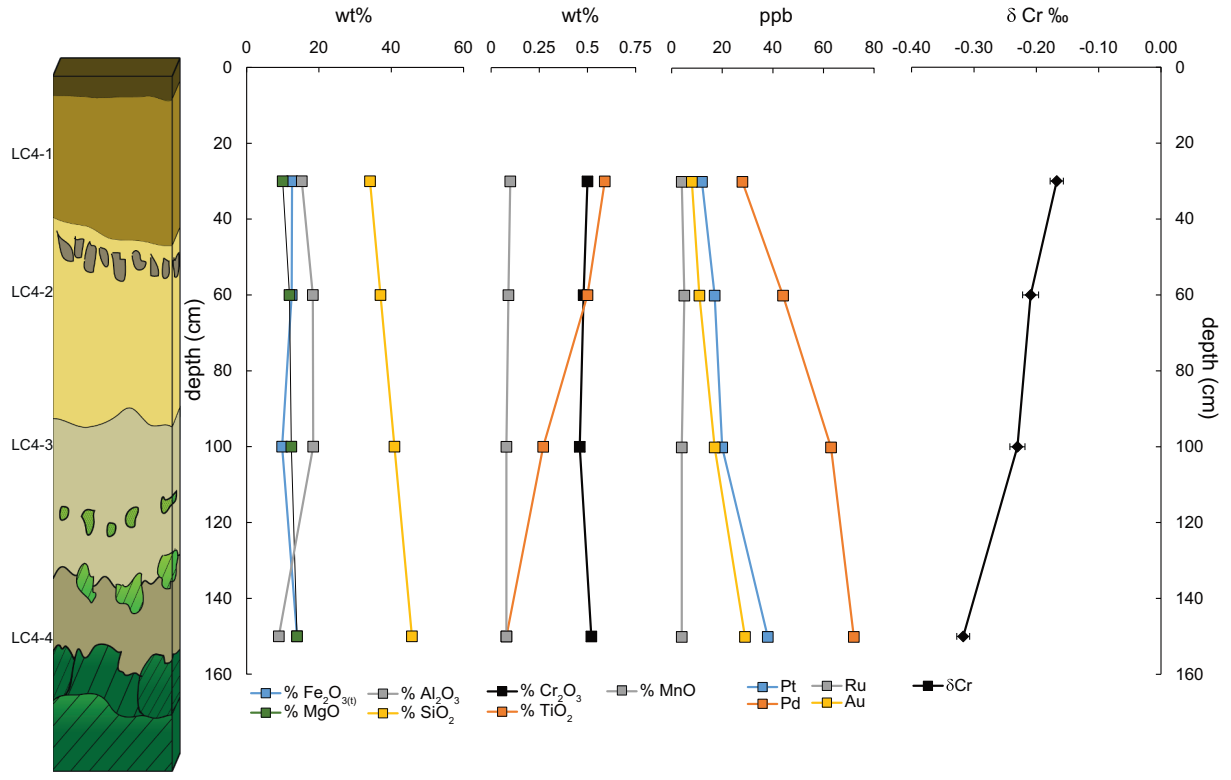

Fig. 5. Bulk major ($Fe_2O_{3\ TOTAL}$, MgO, Al_2O_3 and SiO_2), minor (Cr_2O_3 TiO_2 and MnO) and trace element (Ru + Pt + Pd + Au) contents for LC4 soil profile, located in the north part of the Centinela Bajo body. Additionally, the $\delta^{53/52}$Cr values are shown on the right.

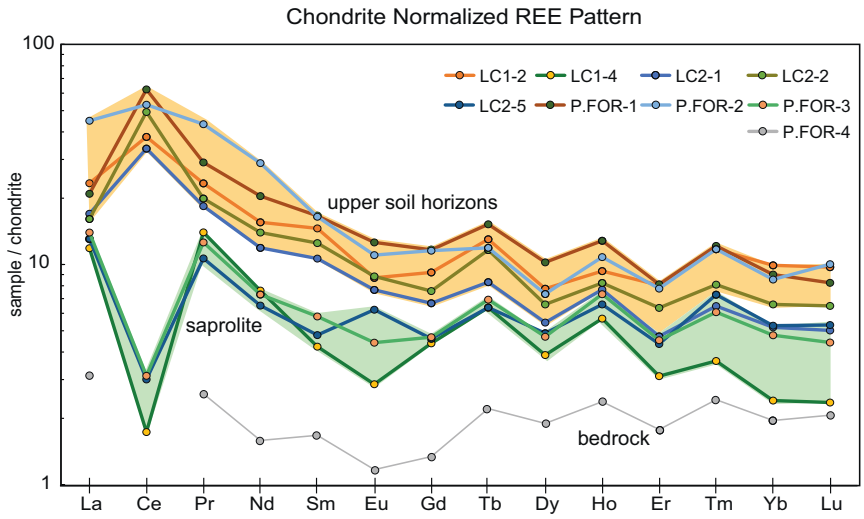

Fig. 6. Chondrite normalized REE pattern for selected samples from soil profiles. Upper soil horizons (yellow) show high LREE contents, contrasting with the saprolite (green) and bedrock contents. (For interpretation of the references to colour in this figure legend, the reader is referred to the web version of this article.)

in the upper horizons. The Ni contents change from 1500 to 2000 ppm in the bedrock to ~500 ppm in upper soil horizons, with the exception of one less developed limonitic soil horizon (e.g., sample P.FOR-3) where a slight increase in Ni content is observed (2370 ppm).

Total rare earth element (REE) contents are higher in the uppermost horizons than in the serpentinite/bedrock and saprolite (Fig. 6, Table 1). The highest contents are reached in the upper limonitic soil horizons from profile P.FOR, with up to 98 ppm of total REE, contrasting with 4 ppm at the bottom of the profile (saprolite). Upper soil horizons from profiles P.FOR, LC1 and LC2, have total REE contents that are one order of magnitude higher than the serpentinite average content. This difference is larger for light REE (LREE; La-Eu) compared to heavy REE (HREE; Gd-Lu) contents, and is punctuated by a positive Ce anomaly in the upper soil horizons (Fig. 6).

4.3. PGE and au contents

Total PGE contents of soil and saprolite samples from La Cabaña range between 17 and 160 ppb (Table 1), with the highest values found in the limonitic soil horizon from profile P.FOR (sample P.FOR-2). In profiles LC2 and LC4, highest PGE (123 and 117 ppb respectively) contents were found in clay-rich saprolite horizons (see profile LC4 in Fig. 5). Among all PGE, Pd and Pt, have the higher contents in soils. Palladium contents range from 2 ppb up to 87 ppb, followed by Pt contents from 4 up to 53 ppb. Ruthenium contents range from 3 to 39 ppb and the other PGE (Os, Ir, Rh) are depleted in these profiles, sometimes below the detection limit (1–5 ppb) (Figs. 4 and 5). It is relevant to note that poorly altered coarse saprolite horizons (Samples LC 1–4 and P.FOR-4) represent the bedrock PGE contents. Gold contents range between 3 and 29 ppb, with slight variations throughout the soil profiles. Interestingly, in the profile P.FOR, there is an increase of Au contents in the limonitic soil horizon, in which Pt, Pd and Ru are also enriched (Fig. 4). In contrast, in profile LC4, the Au content decreases from bottom to top (Fig. 5).

Chondrite-normalized PGE + Au contents in soil and saprolite samples, show an enrichment in the PPGE (Rh + Pt + Pd; Pt-group) and Au, with respect to the serpentinite bedrock (Fig. 7a). Upper limonitic soil horizons of profile P.FOR have also the PPGE enrichment pattern (Fig. 7b), although patterns are less steep than saprolite enrichment patterns of profile LC4.

4.4. Cr stable isotopes

The Cr stable isotope data of samples from La Cabaña are reported in Table 2. All soil samples have negative $\delta^{53/52}Cr_{SRM979}$, within a range

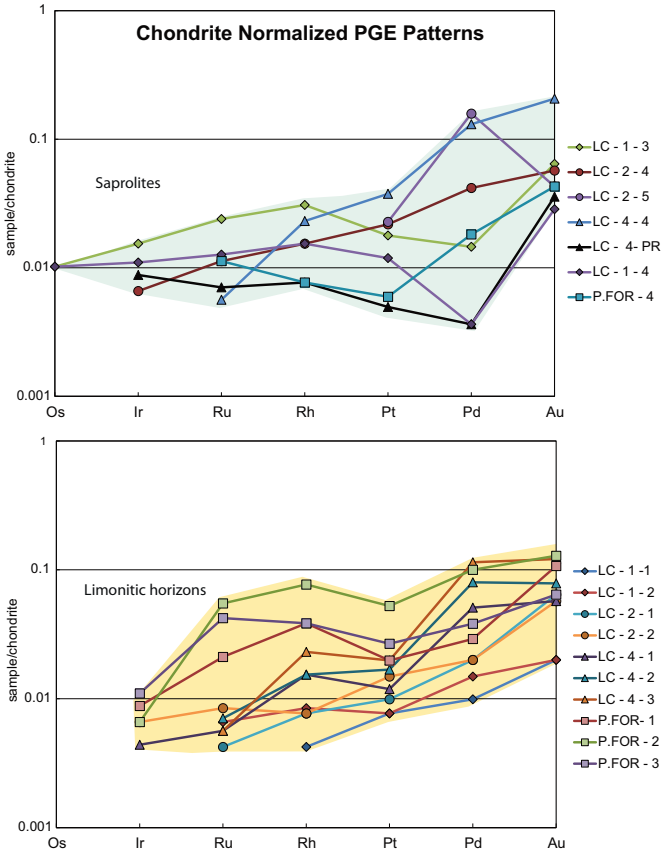

Fig. 7. Chondrite normalized PGE contents of soils from La Cabaña a) Samples show steep trends with Pd and Au enrichment for saprolite, and a relatively flat pattern for serpentinites. B) Enrichment in Pd, Pt and Au in the upper limonitic horizons is also observed, although patterns are less steep than for saprolite. Samples LC – 1–4, P.FOR – 4 and LC – 4 – PR represent the bedrock PGE base contents.

of −0.089 ± 0.012‰ to −0.320 ± 0.013‰ (average of −0.178‰), with the exception of sample LC4–5 (Fe-Mn concretion), which shows a positive $\delta^{53/52}Cr_{SRM979}$ of +0.129‰.

The $\delta^{53/52}Cr$ data show two distinct trends with depth (Figs. 4 and 5). The first trend is represented by soil profiles LC2, LC4 and P.CBS, and is characterized by progressively heavier $\delta^{53/52}Cr$ values towards the top,

Table 2
Cr stable isotope data reported in δ notation from selected soil samples. Errors reported as 2 standard errors.

Sample	Sample type	$\delta^{53/52}$Cr	2SE
LC1-1	Soil	−0.105	0.009
LC1-2	Soil	−0.138	0.013
LC1-3	Soil	–	–
LC1-4	Coarse saprolite	−0.097	0.014
LC2-1	Soil	−0.013	0.007
LC2-2	Soil	−0.161	0.017
LC2-5	Coarse saprolite	−0.169	0.009
LC4-1	Soil	−0.167	0.011
LC4-2	Soil	−0.209	0.013
LC4-3	Soil	−0.230	0.012
LC4-4	Clay saprolite	−0.317	0.010
LC4-5	Fe - Mn Concretion	0.129	0.013
P.FOR-1	Soil	−0.205	0.012
P.FOR-2	Soil	−0.234	0.013
P.FOR-3	Soil	−0.135	0.007
P.FOR-4	Coarse saprolite	−0.089	0.020
P.CBS-1	Coarse saprolite	–	–
P.CBS-2	Coarse saprolite	−0.320	0.012
P.CBS-3	Saprolite	−0.279	0.011
P.CBS-4	Soil	−0.210	0.009
P.CBS-5	Soil	−0.128	0.011
P.CBS-6	Soil	−0.177	0.011

with lighter values for saprolite at the base of the profile (Fig. 5). The second trend, represented by soil profiles P.FOR and LC1, shows an inverse pattern, with $\delta^{53/52}$Cr values decreasing towards the top, with lighter compositions at the limonitic horizons (B horizons) (Fig. 4). A striking feature of this second trend is how the $\delta^{53/52}$Cr values mirror the total PGE and Au contents. In fact, the isotopically lighter values of $\delta^{53/52}$Cr are coincident with the highest contents of PGE and Au along the profiles, especially for Pt and Pd (Figs. 4 and 5, Tables 1 and 2).

5. Discussion

5.1. Degree of weathering of soil profiles

Magnesium and Si are main chemical components of ultramafic rocks, and after weathering they are removed whereas Al and Fe tend to be retained in the soil. This geochemical signature is related to the breakdown of the parent rock mineralogy, followed by the development of secondary minerals such as clay minerals and oxy-hydroxide phases. In order to track the degree of chemical alteration of rocks, weathering indexes are used to quantify the elemental remobilization and characterize the degree of chemical alteration (Babechuk et al., 2014). The Ultramafic Index of Alteration (UMIA, using molar ratios), proposed by Aiglsperger et al. (2016) and the Index of Laterisation (IOL), in wt% from Babechuk et al. (2014), are calculated as:

$$UMIA = 100\,x\,\frac{Al_2O_3 + Fe_2O_{3(T)}}{SiO_2 + MgO + Al_2O_3 + Fe_2O_{3(T)}}$$

$$IOL = 100\,x\,\frac{Al_2O_3 + Fe_2O_{3(T)}}{MgO + SiO_2 + Fe_2O_{3(T)}}$$

These index values illustrate the weathering trend of ultramafic rocks in ternary AF-S-M or A-F-SM diagrams (Al, Fe, Si, Mg respectively, and Fig. 8). UMIA values of soil samples from La Cabaña range from 4.2% to 46.8% and IOL values range from 20.6% to 72.2%. The less weathered, coarse saprolite samples (samples P.FOR-4 and LC 1–4) resemble the bedrock contents with a small degree of weathering, and the higher values are reached at upper limonitic horizons of profile P.FOR, with all sampled profiles following a geochemical trend towards Fe retention (Fig. 8). Overall, the calculated values, are in agreement with an intermediate stage of weathering or moderately "laterised" profile according to the classification proposed by Babechuk et al. (2014).

As weathering progresses, laterite-type soils are formed, and metals released at the weathering front can be incorporated into Fe-Al oxy-hydroxide phases, clays, serpentine and chlorite-type minerals (Butt and Cluzel, 2013). Additionally, residual accumulation of resistant phases also plays an important role as a metal-retention mechanism in lateritic soils (Bowles et al., 2017). At La Cabaña, these two mechanisms may explain the enrichment of precious and transition metals observed in the clay saprolite in profiles LC2 and LC4 (Fig. 5, Table 1). These profiles show a small degree of weathering and are characterized by a high abundance of chromite, ilmenite, rutile and zircon grains in the upper horizons. Furthermore, higher metal contents are noted in Fe-rich soil horizons with characteristic red to yellow-brownish coloration. These features are consistent with the degree of weathering (i.e., UMIA) calculated at the particular depth in the P.FOR profile (Fig. 8) and with the enrichment observed for immobile elements such as Ti, Zr, Hf, Nb

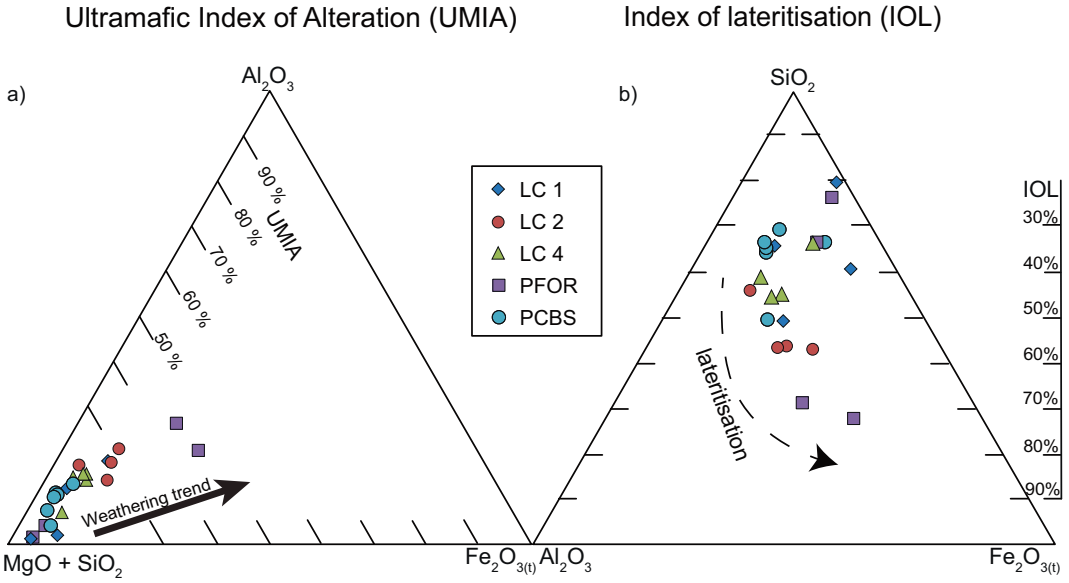

Fig. 8. Weathering trends of soil samples from La Cabaña, showed in ternary diagrams. a) Al_2O_3-Fe_2O_3-($MgO + SiO_2$) space shows Ultramafic Index of Alteration (UMIA) in mole %; b) Al_2O_3-Fe_2O_3- SiO_2 space shows the Index of Lateritisation (IOL) in wt%.

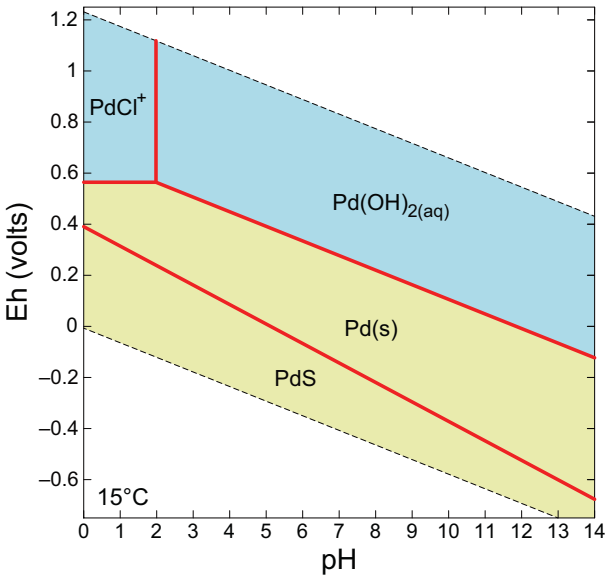

Fig. 9. Eh-pH diagram of Pd species in surface stream water compositions. The light blue field represents aqueous species, and light brown field the solid (mineral) species. a[Pd^{++}] = 10^{-12}; a[HCO_3^-] = $10^{-3.269}$ a[Cl^-] = $10^{-3.793}$; a[SO_4^{--}] = $10^{-5.076}$; a[NO_3^-] = $10^{-48.59}$. The diagram was constructed using Geochemist's Workbench software with provided database including modifications for Pd species according to Wood (1991), Azaroual et al. (2001) and Colombo et al. (2008). (For interpretation of the references to colour in this figure legend, the reader is referred to the web version of this article.)

and Sc, towards upper horizons (Table 1).

Mass balance calculations using tau(τ) factors allow quantifying mass gains and losses of individual chemical elements (Brimhall and Dietrich, 1987; Anderson et al., 2002; Brantley and Lebedeva, 2011) relative to fresh parent rock at La Cabaña. The τ factors were calculated using:

$$\tau_{i,j} = \frac{C_{j,s}/C_{i,s}}{C_{j,p}/C_{i,p}} - 1;$$

where "$C_{j,s}$" is the concentration of an element "j", against the concentration of, an immobile element "i" "$C_{i,s}$" in the soil, normalized by the concentrations of the same elements in the unaltered parent rock ($C_{j,p}$ and $C_{i,p}$). Tau values for Cr against Sc and Ti concentrations are reported in Table 1. Parent rock contents of Cr, Sc and Ti are obtained from data previously reported in González-Jiménez et al. (2016), and also considering contents of the less weathered samples LC 1–4 and P.FOR-4. The $\tau_{Sc,Cr}$ show in general, negative values, despite the increase in Cr concentrations in most of the soil horizons. These results point to a progressive Cr loss in these soils, although the presence of resistant chromite and Cr-magnetite grains suggest relatively slow dissolution kinetics in comparison to other primary phases such as olivine or pyroxene. $\tau_{Ti,Cr}$ values are in agreement with Sc normalized values for profiles P.FOR and LC1, but on the other hand show an opposite trend for profiles LC2 and LC4, where isotopically lighter soil horizons do not have the more negative $\tau_{Ti,Cr}$ values. These differences suggest that resistant minerals (e.g., Fe-Ti oxides, chromite) could be residually accumulated in these profiles, and hence, buffer the Cr isotopic signal.

The chemical patterns observed in the soil profiles at La Cabaña are similar to those reported in more mature lateritic soils, and seem to be controlled by the bedrock lithology, the intensity of weathering and the geomorphological context of the soil profiles (Freyssinet et al., 2005). However, it is important to note that weathering at La Cabaña is incipient and does not show the advanced stages typical of tropical laterites in stable tectonic regions (Thorne et al., 2012; Butt and Cluzel, 2013; Babechuk et al., 2014; Aiglsperger et al., 2016). Despite these limitations, our findings provide insights into the incipient weathering processes affecting ultramafic rocks, and their impact on PGE enrichment and Cr stable isotope fractionation, which are discussed in the next sections.

5.2. PGE and Au enrichment in soils

The noble metal enrichment observed in these soils does not reach the economic grades reported, for example, in Ni laterites of Cuba, Dominican Republic or New Caledonia (Traoré et al., 2008a; Aiglsperger et al., 2015; Aiglsperger et al., 2016). However, PGE and Au enrichment at La Cabaña is noteworthy considering the incipient degree of weathering. The bulk geochemistry of the soil profiles developed above ultramafic rocks at Centinela Bajo reveals different trends of metal enrichment or depletion, showing distinct chemical signals among soil horizons (Figs. 4 and 5). PGE contents in the soils are higher than in the parental rocks, most notably for Pt and Pd (Fig. 7). This enrichment follows two different trends, a saprolite enrichment trend in profiles P.CBS, LC2 and LC4 (Fig. 5), and an upward enrichment trend with higher PGE + Au contents in limonitic soil horizons for profiles LC1 and P.FOR (Fig. 4). In the particular case of sample P.FOR-2 from the P.FOR profile, the total PGE content reaches up to 160 ppb, approximately five times the original bedrock contents. This increase is coupled with an increase in Au, Co, Cr, Cu, Fe, Mn, Sc, and REE contents along the aforementioned profile, also corresponding with the highest calculated degree of weathering (UMIA ~46.8%, Table 1). In contrast, sample LC4-4 from profile LC4 reaches 117 ppb total PGE, but it is not related with high UMIA values. Also, almost no Ir, Os, Ru and Rh are present in LC4 profile, with PGE, Au and Cu contents decreasing towards the top (Table 1 and Fig. 5).

These geochemical trends may reflect local changes in redox conditions in the soil pore space due to rainfall seasonality and long-term precipitation variability, which may affect weathering reactions in La Cabaña. These changes may have an impact on solution-phase reactants, specifically the concentrations of protons, complex (in)organic ligands, and oxidizing or reducing equivalents (Perdrial et al., 2015). Also, some of these changes may be affected by biological activity and the nature of the vegetation cover (e.g, native vs. pine forest). It is relevant to mention that pine plantations developed above P.FOR in the south end of Centinela Bajo (Fig. 2) may have enhanced higher weathering rate at this location, explaining the higher UMIA values in the upper horizon of this profile. Several studies have documented that leaf litter of species from the genus Pinus contains different chemical compounds (e.g., high and low molecular weight organic acids) that can act as acidifying agents, enhancing the chemical weathering of primary minerals (Becerra and Montenegro, 2013; Casanova et al., 2013; Perdrial et al., 2015; Pawlik et al., 2016). However, it is more likely that differences in the degree of weathering at La Cabaña might reflect other factors, including complex tectonic/uplift and climatic feedbacks, which need to be evaluated in detail but are beyond the scope of this paper.

Of particular interest is the relatively high Pd contents in soils at La Cabaña. Fig. 9 shows an Eh vs. pH diagram of Pd species under surface stream water conditions. The gentle slope of the equilibrium between Pd aqueous species $Pd^{+2}(OH)_{2(aq)}$ and a solid phase (Pd(s)) suggests a strong redox control on Pd mobility, with Pd most likely forming hydroxide species ($Pd(OH)_2$) in oxidizing environments such as runoff waters, freshwater and soil solutions (Wood, 1991; Wood et al., 1992; van Middlesworth and Wood, 1999; Azaroual et al., 2001; Colombo et al., 2008; Kubrakova et al., 2011; Reith et al., 2014). The role of pH on Pd release and mobility is less clear, although according to the Eh vs. pH diagram its influence would be limited when compared to redox potential. However, detailed studies of soil and porewater pH must be conducted in the area to evaluate the variations in soil pH above ultramafic blocks, which is estimated to vary between 5 and 5.9 in locations in the Coastal Range close to the study area (Casanova et al., 2013). If ammonia species are present, they could also play an

important role in Pd and Pt mobilization under these conditions (Colombo et al., 2008; Reith et al., 2014). Platinum, may also form aqueous hydroxide species, but is less mobile than Pd at surface environments due to the higher oxidation potential to enter into solution (Sassani and Shock, 1998; Colombo et al., 2008; Reith et al., 2014). The relatively soluble behavior of Pd (and to a lesser extent Pt) at near-surface conditions suggests that Pd may be liberated during the initial stages of weathering from host minerals (PGM, Fe-Ni sulfides and native Au), to be incorporated into pore water as, e.g., $Pd^{2+}(OH)_{2(aq)}$ species and then partially mobilized throughout the soil. This may result in Pd (and Pt) being incorporated or trapped onto clay and oxy-hydroxide-rich soil horizons, or being reduced by Mn or organic matter compounds, due to their high surface area and highly negatively charged interfaces (Bowles, 1986; Gray et al., 1996; Traoré et al., 2008b; Cabral et al., 2011; Kubrakova et al., 2011; Aiglsperger et al., 2015; Aiglsperger et al., 2016). FESEM and SEM observations of heavy mineral concentrates of sample LC4-4 show the presence of Pt minerals (sperrylite and Ru-Os-Ir-Pt-Fe; Fig. 3) and Pt particles associated with porous chromite grains, although no Pd-bearing minerals were observed. In addition, higher Pt contents correspond with higher Sc contents (Table 1), which is a highly immobile element in surficial environments, suggesting that Pt is residually enriched, and is retained as a more resistant phase during weathering. The more soluble Pd, in contrast, is most likely incorporated into very fine grained mineral fractions (Fe hydroxides or clays; Gray et al., 1996; Traoré et al., 2008b), also explaining the difficulty of finding Pd-bearing minerals in soils (Gray et al., 1996).

The morphology and textures of the gold grains found in the sample LC4–4 are characterized by Au refinement towards the rims (Fig. 3). Such textures and chemical features (i.e., lower Ag content) are attributed to the relatively high solubility of Ag compared to Au in oxidizing environments, leading to Ag loss and Au purification (Bowles, 1986, Craw and Lilly, 2016; Stewart et al., 2017, and references within). Considering that the observed gold grains still contain Ag (80 wt% Au–20 wt% Ag) and even some Cu in the cores, it is likely that they were recently liberated from their host rocks, or they were transported only a short distance from the source (Yang et al., 2009; Reith et al., 2012; Stewart et al., 2017). Therefore, the “bulk” Au chemical content of soil horizons at La Cabaña may be related to newly formed Au particles that were further encapsulated by goethite and/or Fe-Mn oxy-hydroxides (Yang et al., 2009, and reference therein).

5.3. Cr isotope isotopes as monitors of PGE enrichment

Since chromium is predominantly hosted by chromite in the ultramafic rocks at La Cabaña, the $\delta^{53/52}$Cr values of the less weathered samples, i.e., low UMIA values (Tables 1 and 2) were taken as the primary isotopic signature of the parent rock (P.FOR-4: -0.089 ± 0.02‰ and LC 1–4: -0.097 ± 0.014‰). These values resemble the global mean value for chromite of $\delta^{53/52}Cr = -0.082 \pm 0.065$‰ (Schoenberg et al., 2008; Farkaš et al., 2013), and are close to the $\delta^{53/52}$Cr value of -0.124 ± 0.101‰ reported for silicate Earth reservoirs or the igneous inventory (Schoenberg et al., 2008; Schoenberg et al., 2016). Hence, it is important to note that the $\delta^{53/52}$Cr values of the studied soils are at least partially buffered by the primary chromite and Cr-rich magnetite grains remaining in the soils (Fig. 5). However, the two distinctive trends of $\delta^{53/52}$Cr vs. depth reported here indicate that soil horizons with the highest PGE contents have the lightest $\delta^{53/52}$C values (Figs. 4 and 5).

During weathering, chromium is released from chromite most likely as $Cr^{+3}(OH)_{3(aq)}$. This compound, could be later oxidized to form chromate species (e.g., CrO_4^{2-}) and either be mobilized out of the soil or back reduced and retained by clay minerals and Fe-Al oxy-hydroxide phases during pedogenesis (D'Arcy et al., 2016; Babechuk et al., 2017; Wille et al., 2018 and references therein). The immobilization of Fe and Al in secondary phases, may also influence the retention of other metals such as Mn, and in some cases, even Pd and Pt (Gray et al., 1996; Aiglsperger et al., 2015). Such interplay of mechanisms of redox transformations and progressive development of secondary phases, are likely to produce isotopic fractionation in modern soils, as reported in previous studies, where the $\delta^{53/52}$Cr values of soils deviate from the bedrock isotopic signal both to lighter and heavier Cr compositions (i.e., $\delta^{53/52}$Cr ranging from -1.29 to 0.5‰; Berger and Frei, 2014; Paulukat et al., 2015; D'Arcy et al., 2016; Novak et al., 2017; Wille et al., 2018). It is well documented that Cr isotopes do not significantly fractionate during oxidation from Cr(III) to Cr(VI) (Izbicki et al., 2008; Zink et al., 2010). However, the reduction of Cr(VI) to Cr(III) leads to isotopic fractionation in the per mil range on the $^{53}Cr/^{52}Cr$ ratio (Ellis et al., 2002; Schoenberg et al., 2008; Zink et al., 2010; Døssing et al., 2011). For this reason, as chromite is weathered and PGE are liberated and subsequently re-concentrated due to redox changes during soil formation, it is likely that such oxidation-reduction reactions have an impact on $^{53}Cr/^{52}Cr$ ratios. Thus, repeated cycles of Cr partial oxidation and partial back-reduction in the soil influence the $\delta^{53/52}$Cr signal of the PGE-enriched soil.

Fig. 10 shows that the highest Pd, Pt, Au and PGE contents are related to the lightest $\delta^{53/52}$Cr signatures. Chromite in the bedrock has relatively low Pd contents, as reported by González-Jiménez et al. (2014a) and González-Jiménez et al. (2016). However, palladium is the most enriched PGE in soils at La Cabaña (Fig. 7), suggesting that Pd liberation and sorption may be related with similar redox mechanisms that affect the liberation/retention of Cr in soils. Experimental data show that Cr reduction by Mn oxy-hydroxides produces a measurable isotopic fractionation towards negative $\delta^{53/52}$Cr values (Schoenberg et al., 2008; Zink et al., 2010). This effect is not restricted to Mn-bearing secondary phases as Fe-bearing species (e.g., magnetite) may cause similar Cr isotopic fractionation (Ellis et al., 2002; Døssing et al., 2011). Considering also that native Au and Pt particles are related with the porous chromite rims and the secondary fine grained PGE mineralization is likely related with the presence of Fe-Mn oxy-hydroxides (Gray et al., 1996; Aiglsperger et al., 2015; Aiglsperger et al., 2016), we argue that the correspondence between lighter $\delta^{53/52}$Cr values and Pd, Pt, Au and total PGE enrichment observed in Fig. 10 is a geochemical signal that monitors the progress of chromite weathering and dissolution, and the amount of Pd and Cr (VI) scavenged by secondary phases in soils such as Fe-Mn oxy-hydroxides.

Studies have shown that when Cr(III) is oxidized and is incorporated into solution as Cr(VI) chromate complexes (CrO_4^{2-}), an isotopically heavier Cr fraction is mobilized leaving a progressively lighter residual $\delta^{53/52}$Cr signature (Frei et al., 2009; Frei et al., 2014). However, it is important to note that the oxidation mechanisms and pathways are not well constrained and further experimental studies are needed (Izbicki et al., 2008; Zink et al., 2010; Døssing et al., 2011). This possible oxidation pathway may leave an isotopically light Cr signal in soil horizons, which may be augmented if an additional back-reduction of solubilized Cr (VI) species modulated by Mn oxides occurs (Ellis et al., 2002; Schoenberg et al., 2008; Zink et al., 2010; Døssing et al., 2011). This mechanism could explain, for example, the $\delta^{53/52}$Cr signature of P.CBS profile, which is an inceptisol with poor development where Mn oxy-hydroxide crusts are observed in the saprolite. Nevertheless, the formation of Fe oxy-hydroxides phases in upper soil horizons, which have high Cr adsorption capacity, may be responsible for the additional back-reduction of Cr if reducing agents are present (e.g., $Fe(II)_{aq}$; Døssing et al., 2011), contributing to the lighter $\delta^{53/52}$Cr signatures in samples with higher Cr contents (e.g., profile P.FOR).

We favor a scenario in which both mechanisms, i.e., oxidation of Cr (III) and back-reduction of Cr(VI), result in soil deviating from the homogeneous $\delta^{53/52}$Cr value of chromite/bedrock (here taken as $\delta^{53/52}Cr - 0.089 \pm 0.02$‰ indistinguishable of $\delta^{53/52}Cr - 0.082 \pm 0.065$‰ by Schoenberg et al. (2008)). In Fig. 11, the $\tau_{Sc,Cr}$ and $\tau_{Ti,Cr}$ values are plotted against the $\delta^{53/52}$Cr data. The results show that lighter $\delta^{53/52}$Cr values are mostly related with negative τ_{Cr} values, i.e.,

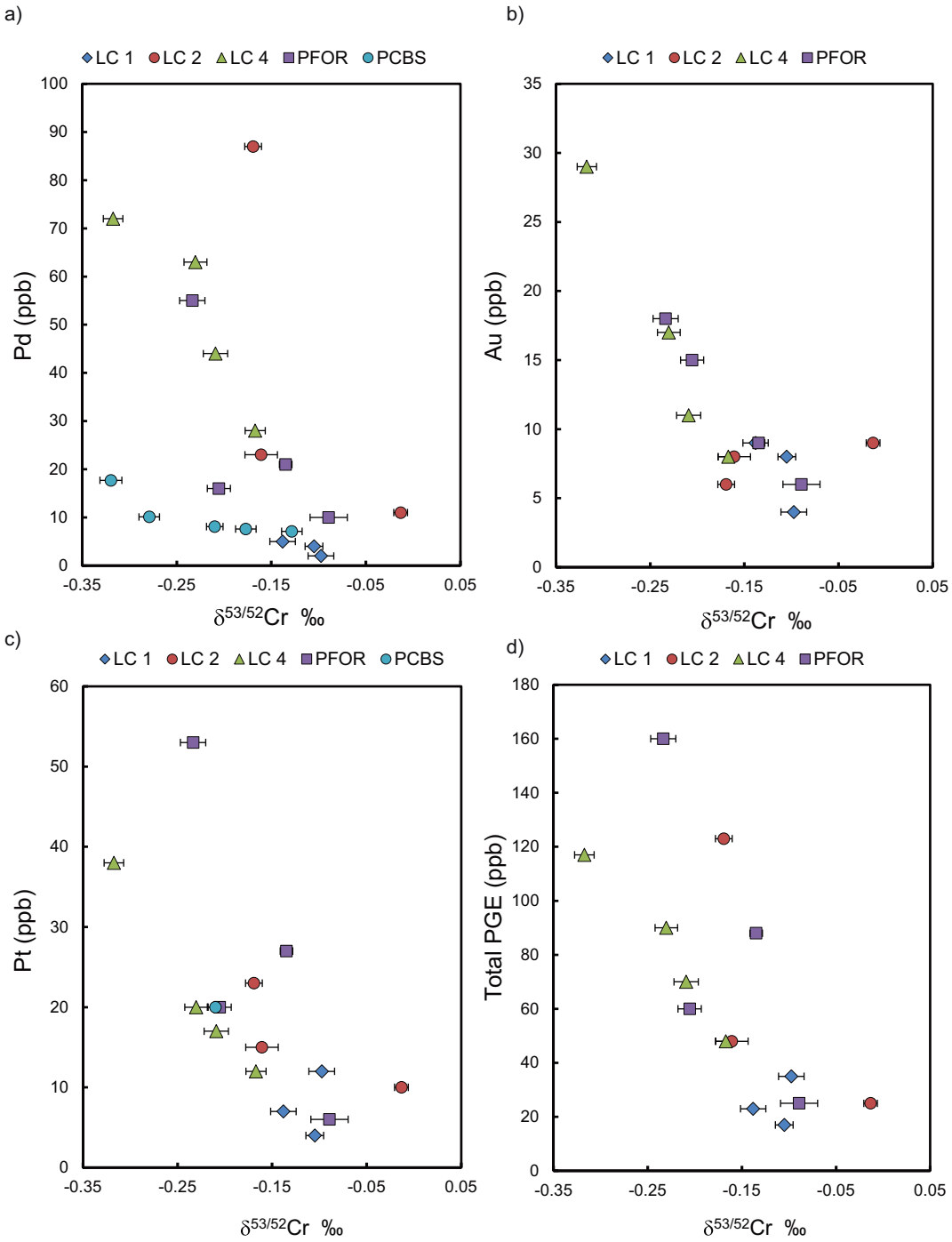

Fig. 10. a, b, c, d) show plots of $\delta^{53/52}$Cr against Pd, Au, Pt and total PGE content, respectively. The lighter $\delta^{53/52}$Cr signature of soil horizons corresponds with higher Pd, Pt, Au, and total PGE concentrations.

higher Cr loss. This suggests that Cr is being removed from the La Cabaña soils, despite the fact that low rates of chromite dissolution and high initial Cr contents may produce a relative enrichment with respect to other elements. The negative τ_{Cr} values corresponding with the lightest $\delta^{53/52}$Cr values support an oxidative weathering model of Cr fractionation (Frei et al., 2009; Frei and Polat, 2013), which produces an isotopic shift to lighter $\delta^{53/52}$Cr values, controlled by the amount of Cr retained at soils as a result of sorption effects modulated by Fe and Mn oxy-hydroxides.

Similar redox-controlled mechanisms have been proposed to explain the stable chromium signatures that are reported in modern soils (Berger and Frei, 2014; Frei et al., 2014; D'Arcy et al., 2016). Even though such mechanisms also explain the slightly positive $\delta^{53/52}$Cr values reported for surficial waters (Izbicki et al., 2008; Frei et al., 2014), further studies are still needed to clarify seasonal effects on $\delta^{53/52}$Cr values of soils and runoff (Novak et al., 2017). Additionally, open-system removal of isotopically light aqueous Cr(III) during pedogenesis has been invoked to explain the $\delta^{53/52}$Cr signature of paleosols where oxidation of Cr(III) and loss of isotopically heavy Cr(VI) is not easily modeled (Babechuk et al., 2017), and recently, non-redox fractionations are reported between Cr(III)-Cl-H_2O aqueous complex (Babechuk et al., 2018) and inorganic ligand promoted dissolution (Saad et al., 2017). Therefore, it is important to keep in mind that the isotopic fractionation of Cr may not be exclusively restricted to redox reactions,

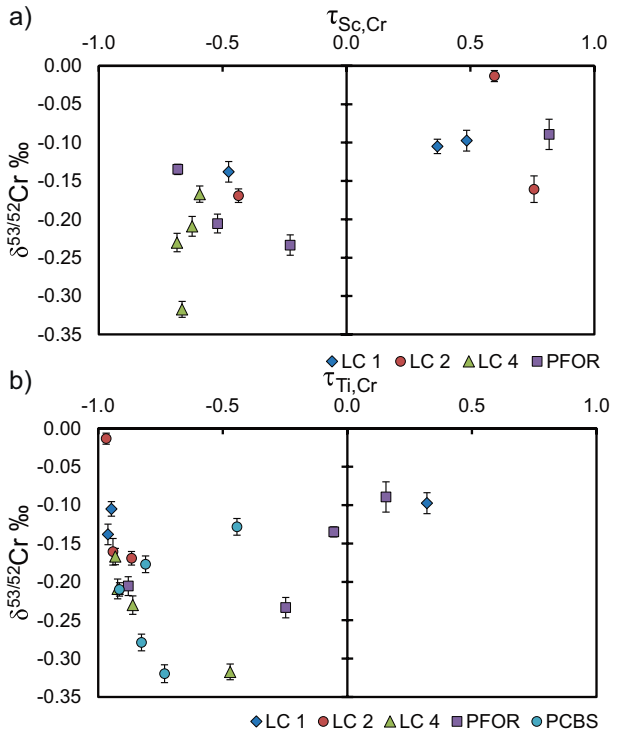

Fig. 11. a) and b) $\tau_{Sc,Cr}$ and $\tau_{Ti,Cr}$ values against $\delta^{53/52}$Cr data respectively. The results show lighter $\delta^{53/52}$Cr in horizons with higher Cr loss (profiles LC1, P.FOR and P.CBS). Profiles LC 2 and 4 also show lighter signatures, but with an opposite trend in which $\tau_{Ti,Cr}$ is relatively higher in those horizons with light $\delta^{53/52}$Cr values.

as widely assumed, and thus non-redox effects should be also taken into consideration in future studies.

6. Concluding remarks

The results presented in this study point to similar metal enrichment patterns as reported for traditional "laterites" developed above ultramafic bodies in tropical latitudes (e.g., Aiglsperger et al., 2015; Aiglsperger et al., 2016). Our data show that the degree of weathering of the La Cabaña soils correspond to an early to intermediate stage of weathering compared to the traditional tropical laterite deposits. Nevertheless, these results provide evidence that important weathering and metal enrichment are not only restricted to tropical latitudes. In fact, pedogenetic processes operating at La Cabaña are capable of increasing the total PGE content of specific soil horizons by several times with respect to the parent rock. This enrichment is not ubiquitous in the study area and seems to be controlled by the parental rock type, the extent of weathering, the geomorphological context of the soil profiles and the type of vegetation. It is important to note that the active tectonics of the Chilean margin is another factor that may impact soil rate formation, modifying weathering/erosion ratios and rearranging the weathering fronts. Future studies should also address the impacts of the recent uplift history of the Coastal Range on soil development.

Chromium isotope systematics were used here as a soil redox proxy due to well-documented fractionation of Cr(VI) to Cr(III) during reduction (Ellis et al., 2002; Schoenberg et al., 2008; Frei et al., 2009; Zink et al., 2010; Frei et al., 2014), which generates a fractionation towards lighter isotopic signatures. Measured $\delta^{53/52}$Cr values show slight variations among the soil profiles (−0.320 to −0.089‰), but most importantly, in Fe-Mn-rich soil horizons, where more negative $\delta^{53/52}$Cr values correlate with PGE and Au enrichment and the intensity of weathering. These results point to a strong redox control on the mobility and sequestration of PGE in the surficial environment, possibly modulated by the presence of Fe-Mn oxy-hydroxides. The results obtained in this study show that Cr stable isotopes, when used in combination with detailed mineralogical and geochemical studies, are a powerful tool for understanding redox cycles during weathering, and the role of secondary phases as potential sinks of important amounts of precious metals in supergene profiles.

Acknowledgments

We acknowledge the Millennium Science Initiative (MSI) grant NC130065 "Millennium Nucleus for Metal Tracing Along Subduction" for providing support for this project, including a M.Sc. scholarship to J. Rivera. Additional support for analytical work at University of Barcelona was provided by the Fondecyt Iniciación Grant #11140005 to JMGJ, and the Spanish projects CGL2015-65824-P and RYC-2015-17596 granted by the Spanish "Ministerio de Economía y Competitividad". We would also like to acknowledge E. Reitter, I. Kleinhaus, M. Wille and R. Romero for their support in the laboratory work. Finally, we thank editor Karen Johannesson for handling the manuscript, and Dave Craw and an anonymous reviewer for their constructive and helpful reviews.

References

Aiglsperger, T., Proenza, J.A., Zaccarini, F., Lewis, J.F., Garuti, G., Labrador, M., Longo, F., 2015. Platinum-group minerals (PGM) in the Falcondo Ni-laterite deposit, Loma Caribe peridotite (Dominican Republic). Mineral. Deposita 50 (1), 105–123.
Aiglsperger, T., Proenza, J.A., Lewis, J.F., Labrador, M., Svojtka, M., Rojas-Puron, A., Ďurišová, J., 2016. Critical metals (REE, Sc, PGE) in Ni laterites from Cuba and the Dominican Republic. Ore Geol. Rev. 73, 127–147.
Aiglsperger, T., Proenza, J.A., Font-Bardia, M., Baurier-Amat, S., Galí, S., Lewis, J.F., Longo, F., 2017a. Supergene neoformation of Pt-Ir-Fe-Ni alloys: multistage grains explain nugget formation in Ni-laterites. Mineral. Deposita 52, 1069–1083.
Aiglsperger, T., Proenza, J.A., Galí, S., Rius, J., Longo, F., Domènech, C., 2017b. The supergene origin of ruthenian hexaferrum in Ni-laterites. Terra Nova 29, 106–116.
Anderson, S.P., Dietrich, W.E., Brimhall Jr., G.H., 2002. Weathering profiles, mass-balance analysis, and rates of solute loss: Linkages between weathering and erosion in a small, steep catchment. Geol. Soc. Am. Bull. 114 (9), 1143–1158.
Azaroual, M., Romand, B., Freyssinet, P., Disnar, J.R., 2001. Solubility of platinum in aqueous solutions at 25 °C and pHs 4 to 10 under oxidizing conditions. Geochim. Cosmochim. Acta 65, 4453–4463.
Babechuk, M.G., Widdowson, M., Kamber, B.S., 2014. Quantifying chemical weathering intensity and trace element release from two contrasting basalt profiles, Deccan Traps, India. Chem. Geol. 363, 56–75.
Babechuk, M.G., Kleinhanns, I.C., Schoenberg, R., 2017. Chromium geochemistry of the ca. 1.85 Ga Flin Flon paleosol. Geobiology 15 (1), 30–50.
Babechuk, M.G., Kleinhanns, I.C., Reitter, E., Schoenberg, R., 2018. Kinetic stable Cr isotopic fractionation between aqueous Cr (III)-Cl-H2O complexes at 25 °C: implications for Cr (III) mobility and isotopic variations in modern and ancient natural systems. Geochim. Cosmochim. Acta 222, 383–405.
Barra, F., Rabbia, O.M., Alfaro, G., Miller, H., Höfer, C., Kraus, S., 1998. Serpentinitas y cromititas de La Cabaña, Cordillera de la Costa, Chile central. Rev. Geol. Chile 25 (1), 29–44.
Barra, F., Gervilla, F., Hernández, E., Reich, M., Padrón-Navarta, J.A., González-Jiménez, J.M., 2014. Alteration patterns of chromian spinels from La Cabaña peridotite, south-central Chile. Mineral. Petrol. 108 (6), 819–836.
Bauer, K.W., Gueguen, B., Cole, D.B., Francois, R., Kallmeyer, J., Planavsky, N., Crowe, S.A., 2018. Chromium isotope fractionation in ferruginous sediments. Geochim. Cosmochim. Acta 223, 198–215.
Becerra, P.I., Montenegro, G., 2013. The widely invasive tree Pinus radiata facilitates regeneration of native woody species in a semi-arid ecosystem. Appl. Veg. Sci. 16 (2), 173–183.
Berger, A., Frei, R., 2014. The fate of chromium during tropical weathering: a laterite profile from Central Madagascar. Geoderma 213, 521–532.
Bowles, J.F., 1986. The development of platinum-group minerals in laterites. Econ. Geol. 81 (5), 1278–1285.
Bowles, J.F., Gize, A.P., Cowden, A., 1994. The mobility of the platinum-group elements in the soils of the Freetown Peninsula, Sierra Leone. Can. Mineral. 32 (4), 957–967.
Bowles, J.F., Suárez, S., Prichard, H.M., Fisher, P.C., 2017. Weathering of PGE sulfides and Pt–Fe alloys in the Freetown Layered Complex, Sierra Leone. Mineral. Deposita 52 (8), 1127–1144.
Brantley, S.L., Lebedeva, M., 2011. Learning to read the chemistry of regolith to understand the critical zone. Annu. Rev. Earth Planet. Sci. 39, 387–416.
Brimhall, G.H., Dietrich, W.E., 1987. Constitutive mass balance relations between chemical composition, volume, density, porosity, and strain in metasomatic hydrochemical systems: results on weathering and pedogenesis. Geochim. Cosmochim. Acta 51 (3), 567–587.
Bucher, K., Stober, I., Müller-Sigmund, H., 2015. Weathering crusts on peridotite.

Contrib. Mineral. Petrol. 169 (5), 52.
Butt, C.R., Cluzel, D., 2013. Nickel laterite ore deposits: weathered serpentinites. Elements 9 (2), 123–128.
Cabral, A.R., Radtke, M., Munnik, F., Lehmann, B., Reinholz, U., Riesemeier, H., Kwitko-Ribeiro, R., 2011. Iodine in alluvial platinum–palladium nuggets: evidence for biogenic precious-metal fixation. Chem. Geol. 281 (1), 125–132.
Casanova, M., Salazar, O., Seguel, O., Luzio, W., 2013. The Soils of Chile. Springer (185 pp.).
Colombo, C., Oates, C.J., Monhemius, A.J., Plant, J.A., 2008. Complexation of platinum, palladium and rhodium with inorganic ligands in the environment. Geochem.: Explor., Environ., Anal. 8 (1), 91–101.
Craw, D., Lilly, K., 2016. Gold nugget morphology and geochemical environments of nugget formation, southern New Zealand. Ore Geol. Rev. 79, 301–315.
D'Arcy, J., Babechuk, M.G., Døssing, L.N., Gaucher, C., Frei, R., 2016. Processes controlling the chromium isotopic composition of river water: constraints from basaltic river catchments. Geochim. Cosmochim. Acta 186, 296–315.
Døssing, L.N., Dideriksen, K., Stipp, S.L.S., Frei, R., 2011. Reduction of hexavalent chromium by ferrous iron: a process of chromium isotope fractionation and its relevance to natural environments. Chem. Geol. 285 (1), 157–166.
Eary, L.E., Rai, D., 1987. Kinetics of chromium (III) oxidation to chromium (VI) by reaction with manganese dioxide. Environ. Sci. Technol. 21 (12), 1187–1193.
Ellis, A.S., Johnson, T.M., Bullen, T.D., 2002. Chromium isotopes and the fate of hexavalent chromium in the environment. Science 295 (5562), 2060–2062.
Farkaš, J., Chrastný, V., Novák, M., Čadkova, E., Pašava, J., Chakrabarti, R., Bullen, T.D., 2013. Chromium isotope variations ($\delta^{53}/^{52}$Cr) in mantle-derived sources and their weathering products: implications for environmental studies and the evolution of $\delta^{53}/^{52}$Cr in the Earth's mantle over geologic time. Geochim. Cosmochim. Acta 123, 74–92.
Frei, R., Polat, A., 2013. Chromium isotope fractionation during oxidative weathering-implications from the study of a Paleoproterozoic (ca. 1.9 Ga) paleosol, Schreiber Beach, Ontario, Canada. Precambrian Res. 224, 434–453.
Frei, R., Gaucher, C., Poulton, S.W., Canfield, D.E., 2009. Fluctuations in Precambrian atmospheric oxygenation recorded by chromium isotopes. Nature 461 (7261), 250–253.
Frei, R., Poiré, D., Frei, K.M., 2014. Weathering on land and transport of chromium to the ocean in a subtropical region (Misiones, NW Argentina): a chromium stable isotope perspective. Chem. Geol. 381, 110–124.
Freyssinet, P., Butt, C.R.M., Morris, R.C., Piantone, P., 2005. Ore-forming Processes Related to Lateritic Weathering: Economic Geology 100th Anniversary Volume. pp. 681–722.
Garreaud, R., Falvey, M., Montecinos, A., 2016. Orographic precipitation in coastal southern Chile: mean distribution, temporal variability, and linear contribution. J. Hydrometeorol. 17 (4), 1185–1202.
Golightly, J.P., 2010. Progress in understanding the evolution of nickel laterites. Soc. Econ. Geol. Spec. Publ. 15, 451–485.
González-Jiménez, J.M., Barra, F., Walker, R.J., Reich, M., Gervilla, F., 2014a. Geodynamic implications of ophiolitic chromitites in the La Cabaña ultramafic bodies, Central Chile. Int. Geol. Rev. 56, 1466–1483.
González-Jiménez, J.M., Barra, F., Garrido, L.N., Reich, M., Satsukawa, T., Romero, R., Plissart, G., 2016. A secondary precious and base metal mineralization in chromitites linked to the development of a Paleozoic accretionary complex in Central Chile. Ore Geol. Rev. 78, 14–40.
González-Jiménez, J.M., Plissart, G., Garrido, L.N., Padrón-Navarta, J.A., Aiglsperger, T., Romero, R., Morata, D., 2017. Titanian clinohumite and chondrodite in antigorite serpentinites from Central Chile: evidence for deep and cold subduction. Eur. J. Mineral. 29 (6), 959–970.
Gray, D.J., Schorin, K.H., Butt, C.R.M., 1996. Mineral associations of platinum and palladium in lateritic regolith, Ora Banda Sill, Western Australia. J. Geochem. Explor. 57 (1–3), 245–255.
Hattori, K.H., Cameron, E.M., 2004. Using the high mobility of palladium in surface media in exploration for platinum-group element deposits: evidence from the Lac des Iles region, northwestern Ontario. Econ. Geol. 99 (1), 157–171.
Hervé, F., 1988. Late Paleozoic subduction and accretion in southern Chile. Episodes 11 (3), 183–188.
Hervé, F., Calderón, M., Fanning, C.M., Pankhurst, R.J., Godoy, E., 2013. Provenance variations in the Late Paleozoic accretionary complex of central Chile as indicated by detrital zircons. Gondwana Res. 23 (3), 1122–1135.
Höfer, C., Kraus, S., Miller, H., Alfaro, G., Barra, F., 2001. Chromite-bearing serpentinite bodies within an arc–backarc metamorphic complex near La Cabaña, south Chilean Coastal Cordillera. J. S. Am. Earth Sci. 14 (1), 113–126.
Izbicki, J.A., Ball, J.W., Bullen, T.D., Sutley, S.J., 2008. Chromium, chromium isotopes and selected trace elements, western Mojave Desert, USA. Appl. Geochem. 23 (5), 1325–1352.
Kubrakova, I.V., Fortygin, A.V., Lobov, S.G., Koshcheeva, I.Y., Tyutyunnik, O.A., Mironenko, M.V., 2011. Migration of platinum, palladium, and gold in the water systems of platinum deposits. Geochem. Int. 49 (11), 1072–1084.
Novak, M., Kram, P., Sebek, O., Andronikov, A., Chrastny, V., Martinkova, E., Myska, O., 2017. Temporal changes in Cr fluxes and δ^{53}Cr values in runoff from a small serpentinite catchment (Slavkov Forest, Czech Republic). Chem. Geol. 472, 22–30.
O'Driscoll, B., González-Jiménez, J.M., 2016. Petrogenesis of the platinum-group minerals. Rev. Mineral. Geochem. 81 (1), 489–578.
Oze, C., Bird, D.K., Fendorf, S., 2007. Genesis of hexavalent chromium from natural sources in soil and groundwater. Proc. Natl. Acad. Sci. 104 (16), 6544–6549.
Paulukat, C., Døssing, L.N., Mondal, S.K., Voegelin, A.R., Frei, R., 2015. Oxidative release of chromium from Archean ultramafic rocks, its transport and environmental impact–a Cr isotope perspective on the Sukinda valley ore district (Orissa, India). Appl. Geochem. 59, 125–138.
Pawlik, Ł., Phillips, J.D., Šamonil, P., 2016. Roots, rock, and regolith: biomechanical and biochemical weathering by trees and its impact on hillslopes-a critical literature review. Earth Sci. Rev. 159, 142–159.
Perdrial, J.N., Thompson, A.A., Chorover, J., 2015. Soil geochemistry in the critical zone: influence on atmosphere, surface-and groundwater composition. Principles and dynamics of the critical zone. Dev. Earth Surf. Process. 19, 173–201.
Reich, M., 2017. Supergene. In: White, W. (Ed.), Encyclopedia of Geochemistry. Encyclopedia of Earth Sciences Series Springer, Cham.
Reich, M., Vasconcelos, P.M., 2015. Geological and economic significance of supergene metal deposits. Elements 11 (5), 305–310.
Reith, F., Stewart, L., Wakelin, S.A., 2012. Supergene gold transformation: secondary and nano-particulate gold from southern New Zealand. Chem. Geol. 320, 32–45.
Reith, F., Campbell, S.G., Ball, A.S., Pring, A., Southam, G., 2014. Platinum in Earth surface environments. Earth Sci. Rev. 131, 1–21.
Reith, F., Zammit, C.M., Shar, S.S., Etschmann, B., Bottrill, R., Southam, G., Brugger, J., 2016. Biological role in the transformation of platinum-group mineral grains. Nat. Geosci. 9 (4), 294–298.
Romero, R., González-Jiménez, J.M., Barra, F., Leisen, M., Garrido, L.N., Talavera, C., Morata, D., 2017. Timing the tectonic mingling of ultramafic rocks and metasediments in the southern section of the coastal accretionary complex of central Chile. Int. Geol. Rev. 1–15.
Saad, E.M., Wang, X., Planavsky, N.J., Reinhard, C.T., Tang, Y., 2017. Redox-independent chromium isotope fractionation induced by ligand-promoted dissolution. Nat. Commun. 8 (1), 1590.
Sassani, D.C., Shock, E.L., 1998. Solubility and transport of platinum-group elements in supercritical fluids: summary and estimates of thermodynamic properties for ruthenium, rhodium, palladium, and platinum solids, aqueous ions, and complexes to 1000 °C and 5 kbar. Geochim. Cosmochim. Acta 62 (15), 2643–2671.
Schoenberg, R., Zink, S., Staubwasser, M., von Blanckenburg, F., 2008. The stable Cr isotope inventory of solid Earth reservoirs determined by double spike MC-ICP-MS. Chem. Geol. 249 (3), 294–306.
Schoenberg, R., Merdian, A., Holmden, C., Kleinhanns, I.C., Haßler, K., Wille, M., Reitter, E., 2016. The stable Cr isotopic compositions of chondrites and silicate planetary reservoirs. Geochim. Cosmochim. Acta 183, 14–30.
Stewart, J., Kerr, G., Prior, D., Halfpenny, A., Pearce, M., Hough, R., Craw, D., 2017. Low temperature recrystallisation of alluvial gold in paleoplacer deposits. Ore Geol. Rev. 88, 43–56.
Taylor, G., Eggleton, R.A., Holzhauer, C.C., Maconachie, L.A., Gordon, M., Brown, M.C., McQueen, K.G., 1992. Cool climate lateritic and bauxitic weathering. J. Geol. 100 (6), 669–677.
Thorne, R.L., Roberts, S., Herrington, R., 2012. Climate change and the formation of nickel laterite deposits. Geology 40 (4), 331–334.
Traoré, D., Beauvais, A., Chabaux, F., Peiffert, C., Parisot, J.C., Ambrosi, J.P., Colin, F., 2008a. Chemical and physical transfers in an ultramafic rock weathering profile: part 1. Supergene dissolution of Pt-bearing chromite. Am. Mineral. 93 (1), 22–30.
Traoré, D., Beauvais, A., Augé, T., Parisot, J.C., Colin, F., Cathelineau, M., 2008b. Chemical and physical transfers in an ultramafic rock weathering profile: part 2. Dissolution vs. accumulation of platinum-group minerals. Am. Mineral. 93 (1), 31–38.
van Middlesworth, J.M., Wood, S.A., 1999. The stability of palladium (II) hydroxide and hydroxy-chloride complexes: an experimental solubility study at 25–85 °C and 1 bar. Geochim. Cosmochim. Acta 63 (11), 1751–1765.
Varajão, C.A.C., Colin, F., Vieillard, P., Melfi, A.J., Nahon, D., 2000. Early weathering of palladium gold under lateritic conditions, Maquiné mine, Minas Gerais, Brazil. Appl. Geochem. 15 (2), 245–263.
Wille, M., Babechuk, M.G., Kleinhanns, I.C., Stegmaier, J., Suhr, N., Widdowson, M., Schoenberg, R., 2018. Silicon and chromium stable isotopic systematics during basalt weathering and lateritisation: a comparison of variably weathered basalt profiles in the Deccan Traps, India. Geoderma 314, 190–204.
Wood, S.A., 1991. Experimental determination of the hydrolysis constants of Pt2+ and Pd2+ at 25 C from the solubility of Pt and Pd in aqueous hydroxide solutions. Geochim. Cosmochim. Acta 55 (7), 1759–1767.
Wood, S.A., Mountain, B.W., Pan, P., 1992. The aqueous geochemistry of platinum, palladium and gold; recent experimental constraints and a re-evaluation of theoretical predictions. Can. Mineral. 30 (4), 955–982.
Yang, Y., Liu, S., Jin, Z., 2009. Laterization and its control to gold occurrence in Laowanchang gold deposit, Guizhou Province, Southwest of China. J. Geochem. Explor. 100 (1), 67–74.
Zink, S., Schoenberg, R., Staubwasser, M., 2010. Isotopic fractionation and reaction kinetics between Cr (III) and Cr (VI) in aqueous media. Geochim. Cosmochim. Acta 74 (20), 5729–5745.